Energy and AI 23 (2026) 100666

Contents lists available at ScienceDirect

Energy and AI

journal homepage: www.sciencedirect.com/journal/energy-and-ai

Edge-cloud artificial intelligence digital twin thermal modeling for rotating sintered core heat pipes

Jialan Liu [a], Chi Ma [b,c,*], Wenhui Zhou [b,c], Mingming Li [d], Jialong He [e], Giovanni Totis [f], Chunlei Hua [g], Liang Wang [g], Gangwei Cui [g], Ruijuan Xue [g], Zhi Tan [g], Jun Yang [h], Kuo Liu [i], Yuansheng Zhou [j], Jianqiang Zhou [k], Shengbin Weng [k]

[a] School of Construction Machinery, Chang'an University, Xi'an 710064, China
[b] College of Mechanical and Vehicle Engineering, Chongqing University, Chongqing 400044, China
[c] State Key Laboratory of Mechanical Transmission for Advanced Equipment, Chongqing University, Chongqing 400044, China
[d] Academy of Aerospace Solid Propulsion Technology, Xi'an 710025, China
[e] Key Laboratory of CNC Equipment Reliability, Ministry of Education, Jilin University, Changchun, Jilin 130022, China
[f] Polytechnic Department of Engineering and Architecture, University of Udine, Via delle Scienze 206, Udine 33100, Italy
[g] Genertec Machine Tool Engineering Research Institute Co., Ltd., Beijing 110142, China
[h] State Key Laboratory for Manufacturing Systems Engineering, Xi'an Jiaotong University, Xi'an, Shaanxi 710049, China
[i] School of Mechanical Engineering, Dalian University of Technology, Dalian, Liaoning 116024, China
[j] State Key Laboratory of Precision Manufacturing for Extreme Service Performance, Central South University, Changsha, Hunan 410083, China
[k] School of Mechanical Engineering, Quzhou University, Quzhou, Zhejiang 324000, China

HIGHLIGHTS

- Digital twin using Simulink for sintered-core heat pipe thermal prediction.
- Simulink and real-world datasets used for transient thermal simulations.
- Experimental validation achieves ±5 % accuracy under varied conditions.
- Digital twin deployed in real time on edge-cloud computing architecture.
- Compared prediction of gradient boosting, neural network, and Transformer models.

GRAPHICAL ABSTRACT

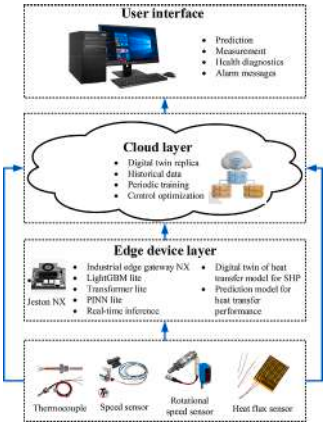

ARTICLE INFO

Keywords:
Physics-informed neural network
Sintered core heat pipe
Thermal prediction

ABSTRACT

The sintered core heat pipe is widely used in precision thermal control and aerospace systems due to its high heat transfer performance. However, conventional computational fluid dynamics approaches for predicting its thermal behavior are computationally expensive and inflexible under varying operating conditions, while

* Corresponding author at: College of Mechanical and Vehicle Engineering, Chongqing University, Chongqing 400044, China.
E-mail address: chima@cqu.edu.cn (C. Ma).

https://doi.org/10.1016/j.egyai.2025.100666

Available online 13 December 2025

Digital twin
Edge-cloud deployment
Rotating heat pipe
Two-phase heat transfer

experimental methods are time-consuming and costly. To address the above challenges, in this study, a digital twin-based predictive thermal modeling framework is presented for sintered core heat pipes under rotational conditions, implemented within an edge-cloud artificial intelligence architecture. A fully parameterized physical model is developed on the Simulink platform using the SIMSCAPE Fluids module, enabling dynamic simulations of phase transitions and temperature responses. Validation against experimental data shows prediction errors within ±5 %. Simulation and experimental datasets are integrated to train three models-physics-informed neural network, Transformer, and light gradient boosting machine-evaluated under steady and transient thermal conditions. The physics-informed neural network achieves the lowest mean absolute error of 0.85 °C in high thermal inertia cases, while the Transformer attains the best steady-state accuracy with a root mean square error of 0.58 °C and inference latency of 150 ms after Turing Tensor R-Engine deployment. Docker-based deployment enables real-time edge inference, with the Transformer achieving an optimal balance of accuracy, memory footprint (36 MB), and response speed. The proposed framework offers a practical and scalable approach for accurate thermal prediction in advanced thermal management applications.

Nomenclature

$\dot{m}$	mass transfer rate
R_u	universal gas constant
p	vapor pressure
m_v	vapor mass
R^*	complete gas constant of the vapor
V	volume of the tank
γ	multidirectional exponent
R_u	universal gas constant
M	molar mass of the vapor
V_v	vapor volume
T_v	absolute vapor temperature
ρ_l	gas mass density
r_w	outer radius of rotation path
h_{lv}	latent heat of vaporization/condensation
r_v	vapor cavity radius
l_{eff}	effective heat transfer length
ε	porosity of the sintered core
K	permeability of the sintered core
σ	surface tension of liquid,
r_{eff}	effective capillary radius of wick pores;
Δp_{grav}	denotes the gravitational pressure head
M	mass of the fluid in the pipe
ϕ_A	passage of energy via port A into the pipe
ϕ_B	passage of energy entering the pipe via port B
h_{coeff}	average convective heat transfer coefficient
T_H	pipe's wall temperature
μ_v	vapor dynamic viscosity
r_v	vapor core radius
R_{wick}	conduction resistance across the porous wick
R_{cond}	and condenser-side condensation resistance
ρ_l	density of liquid
S_m	phase-change mass source term
$\vec{a}_{cent} = w^2 r\hat{r}$	centrifugal acceleration vector
r	radial distance from axis of rotation
θ	contact angle
h_l	is the specific enthalpy of the liquid
$\dot{q}_{gen}$	internal heat generation
T_{ave}	each temperature measurement point's time-averaged temperature
T_h	is the average temperature of T0-T2
λac	thermal conductivity
ΔHac	thickness of the insulating cotton
g	parameter value of acceleration of gravity
d	outer diameter
h	convective heat transfer coefficient
w	weights
w	rotational speed
z	axial position
P_{vapor}	vapor channel axial pressure
T_{wall}^{local}	transient wall temperature at selected sensor positions
ρ	density
ρ_v	density (vapor phase)
σ	surface tension
k_l	thermal conductivity (liquid)
Tsim	simulated temperature
Tsim-T0	temperature difference between Tsim and T0
Tsim-T2	temperature difference between Tsim and T2
s	operating parameters
$\hat{u}(x,t)$	axial liquid velocity in wick
λ_1 and λ_2	weighting coefficient
Γ_{energy}	partial differential equation (PDE) residual for the energy
N_y	labeled temperature points
$\hat{u}$	predicted axial liquid velocity in the wick
h_{fg}	latent heat
ρ	density
$\dot{m}$	phase-change mass flow rate
z^*	normalized variable of axial position z.
t^*	normalized time
w^*	normalized rotational speed
Led^*	normalized Led.
$\hat{T}_{peak,i}^{sim}$	simulation result
MAE	mean absolute error
R	correlation coefficient
F	set of all features
$\|S\|$	the number of features in subset S
$f_{S\cup\{j\}}$	model output when using only features in subset S as input $x_{S\cup\{j\}}$
$\frac{\|S\|!(\|F\|-\|S\|-1)!}{\|F\|!}$	Shapley weight
T_{acq}	the sensor data acquisition delay
T_{comm}	network communication delay
$FLOPs$	number of floating-point operations required by the model;
λ	fixed initialization or loading overhead
T_{cycle}	control loop sampling period
η	learning rate
SHP	sintered core heat pipe
TP	thermal performance
HTP	heat transfer performance
MSE	mean square error
Tensor R-Engine	TensorRT
PINNs	physics-informed neural networks
GAN	generative adversarial network
API	application programming interface
DC	direct current
SiLU	Sigmoid linear unit
MAE	mean absolute error

MQTT	message queuing telemetry transport
ONNX	open neural network exchange
FLOPs	floating-point operations
MLP	multilayer perceptron
p	pressure
M_v	molar mass of the vapor
V_v	vapor volume
T_v	absolute temperature
t	time
T	temperature
Q	input thermal power
m_v	mass of vapor in evaporator plenum
p_v	is vapor pressure
Z	compressibility factor
M_{li}	mass of liquid in volume of sintered core
μ_l	dynamic viscosity of liquid
r_v	inner radius of rotation path
ρ_v	gas mass density
μ_v	vapor dynamic viscosity
M_{li}	mass of liquid in the sintered core
v	flow rate
A_w	cross-sectional area of the liquid flow
θ	contact angle
Δp_v	pressure drop in vapor core;
$\Delta P_{centrifugal}$	centrifugal pressure head
u_{out}	specific internal energy
Δz	parameter value
Q_H	heat entering pipe through port H's wall
S_{surf}	surface area of the pipe
T_I	is the fluid's temperature inside pipe
Q_v	volumetric flow rate
R_{evap}	evaporator-side boiling resistance
R_{vapor}	vapor transport resistance
ε	porosity of sintered core
$\vec{v}_l$	Darcy velocity
k	permeability
μ_l	dynamic viscosity
σ	surface tension;
r_{eff}	effective pore radius of sintered matrix
k_{eff}	is the effective thermal conductivity of the porous wick
$\dot{q}_{phase}$	latent heat source term
Tt	acquisition temperature
T_c	the average temperature of $T5 - T7$
Aac	wrapping area
ΔTi	temperature difference
Δz	parameter value of gain from port A to port B
l_h	length of evaporating section
i	number of hidden layer nodes
Y	data values
FR	liquid filling ratio
x	evaporator vapor mass
ΔP_{wick}	wick core pressure drop,
c_p	specific heat capacity
k	thermal conductivity
$c_{p,l}$	specific heat capacity (liquid)
ρ_l	density (liquid phase)
μ_l	dynamic viscosity
Tsim-T1	temperature difference between Tsim and T1
Tsim-T3	temperature difference between Tsim and T3
$\widehat{T}(x,t)$	temperature
$\widehat{p}(x,t)$	vapor pressure
Γ_{data}	data residual
$\Gamma_{momentum}$	partial differential equation (PDE) residual for momentum equations
$\widehat{T}$	predicted temperature
α	effective thermal diffusivity
A	denotes the flow cross-section;
c_p	specific heat
x^*	normalized variable of vapor mass x
Q^*	normalized heat input
FR^*	normalized filling rate
$\widehat{T}_{peak,i}$	measured temperature
$\overline{T}^{sim}_{peak,i}$	average of simulation result
R^2	R-square
ϕ_j	Shapley value of feature j
S	subset of features that does not include feature j
$\lvert F\rvert$	the total number of features in the full set F
$f_{S\cup\{j\}}\left(x_{S\cup\{j\}}\right)$	model output when feature j is added to subset S
T_k	the k^{th} regression tree
d_k	dimension of the key vectors
Q, K, and V	query, key, and value matrices
T_{proc}	inference time depending on model complexity
T_{sync}	asynchronous queuing or synchronization delays
ν	hardware-dependent scaling factor
M_m	model memory size
δ	minimal margin (e.g., 50 ms) required for safe feedback control
HP	heat pipe
HT	heat transfer
HTM	heat transfer model
RMSE	root mean square error
ANN	neural network model
CFD	computational fluid dynamics
PIML	physics-informed machine learning
LightGBM	light gradient boosting machine
AI	artificial intelligence
1D	one-dimensional
SHAP	SHapley Additive exPlanations
PDE	partial differential equation
Adam	adaptive moment estimation
RMSE	root mean square error
GPU	graphics processing unit

1. Introduction

Because of their high thermal conductivity, near-isothermal properties, and passive operation, heat pipes (HP) [1], which are effective two-phase heat transfer (HT) devices [2], have shown notable benefits in energy recovery [3], electronics cooling [4], and aerospace applications [5]. The application of HP shows significant potential in other fields, including military technology, machine tool, and etc. [6]. To guarantee functional efficacy, HP's thermal performance (TP) must be assessed at the design phase. This evaluation is typically conducted through experimental measurements and numerical simulations. As modern applications demand higher power densities, miniaturization, rotation, and operation under extreme conditions [7], traditional empirical models increasingly fail to predict thermal behavior under multi-parameter coupling scenarios. Numerical simulations have become a common alternative. However, methods based on computational fluid dynamics (CFD) are highly time-consuming and computationally expensive, especially when modeling complex gas-liquid two-phase flows. Experimental methods, while accurate, are costly and time-consuming. The complexity and duration of testing procedures

limit their practicality for iterative design and optimization. Moreover, the HT data under rotating conditions is scarce. These limitations reduce their suitability for rapid TP evaluation in practical engineering design. Therefore, there is an urgent need to develop predictive models that offer high accuracy and computational efficiency. Such models are essential for supporting optimal heat pipe design and ensuring performance reliability under diverse and challenging operating conditions.

In recent years, extensive research has been conducted on the operating mechanisms and HT characteristics of HP [8]. On the one hand, theoretical investigations have primarily focused on modeling, simulation, and qualitative analysis of internal fluid flow and phase change behavior. On the other hand, experimental research has been used to attempt to measure how important design and implementation parameters affect TP. To estimate HP's HT capacity, a number of prediction models have been put forth [9]. Mechanistic models-such as distributed parameter models and capillary-gravity synergy models-have been developed based on HT and fluid dynamics theories. To demonstrate the impact of variables like pipe length, filling ratio, and inclination angle on HT limits, these models discretize the internal phase change processes. To simulate multiphase flow and HT in sodium HP, an enhanced volume-of-fluid technique was presented in conjunction with a multiregional modeling framework [10]. Both experimental and numerical techniques were used to investigate the TP of high-speed radial rotating HP under various centrifugal accelerations and thermal loads [11]. A droplet condensation model for coreless HP was developed, incorporating vapor backflow effects to investigate dynamic characteristics and HT coefficients under different operating conditions [12]. A transient HP model that considered spatiotemporal variations in wick saturation was constructed [13]. Data-driven approaches have also been explored. To forecast the effectiveness of retinal wick HP, K-nearest neighbors, Kriging, and radial basis function interpolation were employed [14]. To predict HT features based on a variety of input parameters, deep learning models, such as artificial neural networks (ANN), were used [15]. ANN-based predictive control system was developed for regulating power in HP-cooled reactors [16]. A grey system model was used to simulate the performance of axial rotating oscillating HP [17], while a fusion prediction model was proposed for radial rotating oscillating HP [18].

The sintered core heat pipe (SHP) has been reported to exhibit significantly better heat transfer performance (HTP) than radial rotating and axial rotating oscillating HPs. As a result, the design optimization and accurate TP evaluation of SHP are of particular importance. However, existing prediction models for SHP still face major limitations. For example, the experimental study about the heat transfer performance is unable to extend to other working conditions [19]. The numerical simulation method is time-consuming and costly [20]. The data-driven ANN method faces the challenge to get enough dataset for model training [21]. The machine learning method also shows difficulty in getting enough dataset for model construction [22]. So far, there has been no report on the HTP evaluation method for the SHP in rotational working environments. In particular, their accuracy deteriorates under complex working conditions involving multiple interacting factors. Under extreme environments-such as high temperature and high pressure-the coupled effects of phase transition dynamics and material thermal stress lead to nonlinear behaviors that are difficult to be modeled precisely. Although numerical methods can estimate the maximum HT capacity under steady-state conditions, most simulation approaches, such as those based on Fluent, rely on transient computations that simulate the entire process from start-up to steady operation. These simulations must account for the time-dependent evolution of two-phase flow and HT characteristics. Consequently, the simulation period is long and the computing load is significant. In addition, accurate modeling of dynamic vapor-liquid interactions and phase interface tracking further increases computational complexity. Therefore, although such models offer physical insight, they lack efficiency and are unsuitable for iterative design or real-time evaluation. Experimental methods are capable of capturing real-world HT behavior, but the associated costs are high. Furthermore, their accuracy cannot be guaranteed when only limited data are available. In industrial applications, where rapid and cost-effective design iterations are required, these limitations prevent experimental or traditional numerical models from serving as practical predictive tools. Consequently, there remains a critical need for reliable, efficient, and generalizable prediction methods to support the optimal design and application of SHP under varied and demanding conditions [23]. This conclusion is consistent with that shown in [24].

Due to the complex internal flow and phase-change HT mechanisms in SHP, their TP is highly sensitive to design and operating parameters. Therefore, developing a fast and reliable method to determine the optimal combination of these parameters is critical for industrial deployment. Previous experimental studies have proposed semi-empirical correlations based on specific structural and operational conditions. These correlations, typically obtained through curve fitting, can reasonably be used to predict HTP within the tested range and often show good agreement with experimental results. However, these models generally lack generalization capability and robustness. They are unable to capture the complex multi-parameter interactions that occur in real-world applications, making them unsuitable for rapid optimization across diverse working conditions. Recently, ANNs have been increasingly adopted in HP modeling due to their strong nonlinear mapping and self-learning capabilities. Compared with high-fidelity CFD simulations and repeated experimental campaigns, which require extensive computational or laboratory resources for each new operating condition, the proposed ANN-based framework offers a fundamentally different cost profile. A one-time offline training process, using a hybrid dataset that integrates validated SIMSCAPE-generated data with limited targeted experiments, enables the model to deliver millisecond-level predictions. This allows real-time deployment in rotational SHP applications where the prediction latency must be within 100–200 ms for effective control actions. The ability to generalize across a broad range of thermal loads, rotational speeds, and filling ratios makes the ANN framework a practical choice for predictive thermal modeling in scenarios where data collection is costly and rapid inference is essential. By learning from data, ANN can be used to predict performance based on known structural and operational parameters without requiring explicit physical formulations. For SHP, ANN-based models can provide a data-driven alternative to traditional physical modeling, offering improved flexibility and reduced experimental cost. In recent years, the intelligent thermal prediction models have drawn increasing attention. Several studies have explored the use of artificial intelligence (AI)-based approaches for thermal prediction. Recent advancements in machine learning for heat transfer and two-phase systems include three notable directions. Recently, the physics-informed neural networks (PINNs) are used. For example, PINNs were applied to complex heat transfer scenarios where conventional methods struggle, by incorporating governing equations directly into model training [25]. More comprehensive reviews outlined PINN applications across engineering scales and affirmed their capability for enhancing physical fidelity and data efficiency [26]. For physics-informed machine learning (PIML), the integration of physics-informed models for surrogate modeling was reviewed in the area of additive manufacturing-where limited data and complex physics coexist-highlighting efficiency and reliability advantages [27]. For physics-informed generative AI, a generative adversarial network (GAN) framework informed by physics was proposed to solve multiphase flow equations within noisy environments, demonstrating forward and inverse modeling with embedded conservation principles [28]. Additional evidence showed AI techniques facilitating feature extraction and predictive modeling in phase-change heat transfer [29]. Such approaches are increasingly adopted in high-precision manufacturing sectors worldwide, including semiconductor fabrication in East Asia, aerospace engineering in North America, and high-speed transportation systems in Europe.

The development of high-fidelity predictive models for rotating SHPs has direct implications for energy-efficient thermal management in advanced systems. In settings such as aerospace avionics, electric vehicle thermal modules, and concentrated solar thermal systems, real-time predictive thermal control can significantly reduce energy consumption by minimizing both heat losses and active cooling power. Embedding an edge-cloud AI framework enables adaptive inference and control, aligning SHP performance with global energy-AI optimization trends toward smart, sustainable thermal systems. Recent studies demonstrate growing integration of AI techniques within energy-related thermal systems. For example, a PIML method was employed to estimate time-varying heat transfer coefficients in solar-thermal collectors with high accuracy and physical consistency [30]. These trends underscore the strong relevance of AI-driven thermal modeling to energy systems. However, most existing solutions remain limited to offline computation, and few are compatible with embedded or resource-constrained hardware environments. The emerging trend of edge-cloud collaborative architectures offers a promising direction for deploying lightweight models to perform inference near the data source while offloading complex analytics to the cloud. Despite this, research on model quantization, latency optimization, and real-time communication for thermal-aware prediction systems is still scarce. Moreover, the deployment of physics-informed or transformer-based models in embedded edge environments-particularly under complex transient thermal loads-remains largely unexplored. These challenges highlight the need for a unified, deployment-oriented framework that bridges predictive modeling with system-level integration.

It is concluded that the heat transfer simulation of heat pipes can be categorized into steady-state and dynamic simulations. The CFD method used in this study is a dynamic simulation approach. Although this method can demonstrate the maximum heat transfer capacity of the heat pipe under stable operating conditions, Fluent-based simulations typically employ transient calculations that require modeling the entire process from startup to steady state, involving time-dependent flow and heat transfer characteristics. This results in high computational complexity and cost. Additionally, Fluent simulations demand precise modeling of the dynamic behavior of the gas-liquid two-phase flow inside the heat pipe and tracking of the phase interface evolution, which further increases the difficulty and duration of computations. Based on the above analysis, the following research gaps are identified:

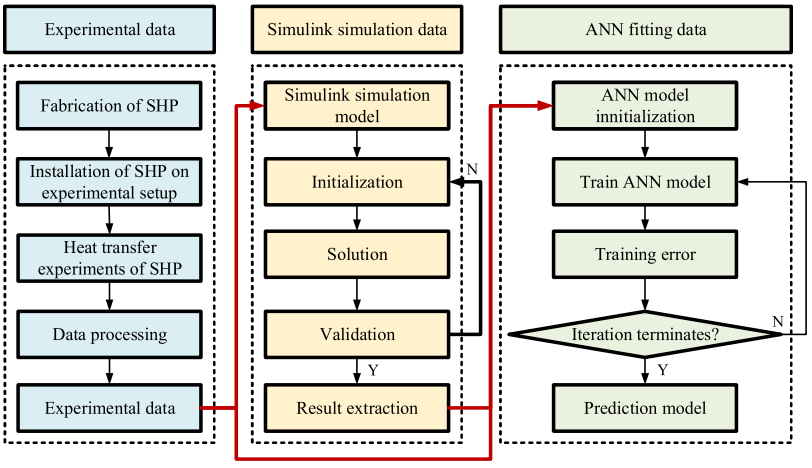

(a)

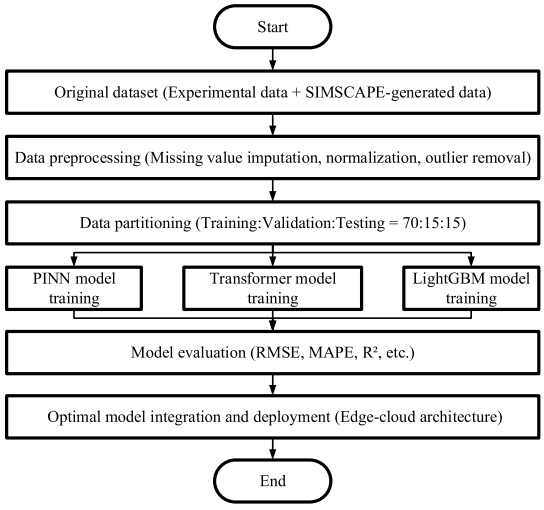

(b)

Fig. 1. Technical route (a) Experiment-simulation-ANN modeling logic diagram of neural network model. The experimental data and the Simulink simulation data are combined to be used as generate the input data of the ANN model. The Simulink simulation data is verified by the experimental data to guarantee the reliability of the ANN model. (b) Workflow of the artificial intelligence-driven thermal modeling pipeline, illustrating data acquisition from experiments and simulations, preprocessing, model training, and deployment within the edge-cloud architecture for real-time heat pipe performance prediction.

(1) Most existing studies rely on CFD for modeling HP performance, which is time-consuming, computationally expensive, and often lacks modular flexibility. There is no existing literature reporting a Simulink-based simulation framework that enables dynamic, physics-informed modeling for SHP. Machine learning-based prediction models often suffer from high data dependency and limited training robustness, which restrict their applicability when large-scale, high-quality datasets are unavailable. Data-driven approaches typically require large-scale, high-quality datasets, which are often difficult and costly to be obtained experimentally. There is a critical need for a hybrid framework that integrates simulation-generated data with experimental results to enhance ANN training and improve prediction accuracy.
(2) Most existing approaches rely on conventional data-driven models that lack physical interpretability and struggle to generalize across variable operating conditions, particularly under transient heat disturbances. Existing models often fail to maintain accuracy across varied structural and operational configurations, especially under extreme or coupled boundary conditions. They lack the adaptability required for robust design guidance in practical engineering applications. Moreover, while PINNs and Transformer architectures have shown promise in other thermal or dynamical systems, their application to rotating SHP has not been explored.
(3) Few studies consider practical deployment constraints-such as inference latency, model size, and resource limitations-which are essential for real-time thermal prediction. Moreover, the integration of Simulink-based digital twins with AI-driven prediction frameworks remains underdeveloped, especially in the context of hybrid edge-cloud architectures. These gaps motivate the development of a physics-guided, deployment-aware framework that bridges modeling fidelity and real-time applicability.

Therefore, to more efficiently obtain the HTP of the SHP under steady-state operation across different working conditions, in this study, a SHP simulation model based on Simulink is established and transient simulations are conducted in combination with computational procedures. This aims to study the heat transfer characteristics of the heat pipe under various conditions to expand the dataset required for training the neural network model. By integrating simulation data with experimental data, a neural network method is employed to develop a predictive model for the heat transfer performance of the SHP, providing a valuable reference for rapid evaluation of heat pipe performance in engineering applications. Then the concept of this study is generated. The technical route of this study is structured around the goal of achieving high-fidelity, real-time thermal prediction for SHP under rotational working conditions, as shown in Fig. 1. First, a digital twin of the drive mechanism is established using Simulink, incorporating heat conduction, rotating heat source characteristics, and SHP cooling effects. This model is validated via experimental measurements and used to generate synthetic datasets covering both steady-state and transient thermal conditions. Second, three predictive models-PINN, Transformer, and light gradient boosting machine (LightGBM)-are constructed and trained using a hybrid dataset. The PINN captures underlying physics, while Transformer focuses on temporal feature learning. Third, multi-scenario test cases are designed, including stepwise thermal load increase, spindle speed ramp-up, and combined fluctuations, to comprehensively evaluate model robustness and accuracy. Finally, the models are deployed in an edge-cloud architecture. Transformer and LightGBM are quantized and deployed on Jetson Xavier using Tensor R-Engine (TensorRT) and application programming interface (API), while PINN is containerized with Docker. Real-time inference latency, model footprint, and system response are evaluated to verify the practical applicability of the proposed framework in embedded intelligent systems. Compared to existing works, the proposed approach leverages a hybrid dataset-combining SIMSCAPE-generated simulations with targeted experiments-to train three edge-deployable models (PINN, Transformer, LightGBM), maintained within a physically consistent and real-time-ready AI framework. This fills a gap in current literature by aligning physical interpretability with deployment efficiency. The proposed framework is able to enhance this by combining hybrid simulation-experimental datasets with real-time edge-cloud deployment, tailored to SHPs-a domain particularly critical for compact, energy-intensive applications. The main contributions of this work are summarized as follows:

(1) This work is the first to develop a fully parameterized digital twin of a rotating SHP using the Simulink platform with SIMSCAPE Fluids, capturing rotational thermal loads, contact conduction, and phase change phenomena.
(2) A combined physical-experimental dataset is used to train advanced AI models (PINN, Transformer, LightGBM), achieving robust predictions in both steady and transient thermal regimes while alleviating data dependency.
(3) The predictive framework is embedded in an edge-cloud architecture with TensorRT acceleration and Docker containerization, enabling sub-150 ms inference latency and compact model size, demonstrating feasibility for on-machine real-time thermal error compensation.

The structure of this document is as follows: In Section 2, the Simulink platform is used to create high-fidelity digital twin of heat transfer model for SHP. Moreover, the theoretical model of heat transfer model for SHP is proposed to verify the effectiveness of the digital twin of heat transfer model. Besides, the experimental setup and validation of simulation results under different design and operating parameters are presented. In Section 3, the construction and training of the PINN, Transformer, and LightGBM based on combined simulation and experimental data are described. In Section 4, the edge-cloud AI architecture for digital twin-based predictive thermal modeling of SHP under rotational conditions is designed. Moreover, its validation is conducted. In Section 5, the study is concluded and the key findings are summarized.

2. Digital twin of heat transfer model for SHP

The decision to employ SIMSCAPE-generated data, rather than relying solely on experimental datasets or generative AI-based augmentation, is made for three key reasons. First, the developed SIMSCAPE model is a physics-based, component-level representation governed by conservation of mass, momentum, and energy, and is calibrated against measured thermal responses for multiple rotational speeds and thermal loads. This ensures that essential nonlinear phenomena-such as centrifugal-force-induced liquid return, variable phase-change rates, and rotationally modulated capillary limits-are preserved in the simulations. Second, while direct experimental measurement offers the highest physical realism, it is constrained by high cost, limited test time, and equipment safety concerns in extreme operating regimes (e.g., $>$300 r/min or low filling ratios). The SIMSCAPE framework allows us to safely explore such conditions and to generate dense, wide-coverage datasets without compromising physical consistency. Third, unlike generative AI augmentation methods, which may produce statistically plausible but physically inconsistent samples, SIMSCAPE outputs are inherently constrained by governing equations, making them more suitable for training physics-informed or hybrid AI models. Furthermore, this simulation-first approach enables a smooth transition to the subsequent AI modeling stage. The SIMSCAPE-generated datasets serve as the primary training resource for the three predictive models-PINN, Transformer, and LightGBM-while targeted experimental data are incorporated to fine-tune and validate these models under real-world conditions. This hybrid data strategy ensures that the trained AI models combine broad coverage across the operating envelope with strong physical grounding, thereby enhancing both

predictive accuracy and generalization capability in the edge-cloud deployment framework.

2.1. Simulink-based modeling and prediction

In this work, MATLAB Simulink with the SIMSCAPE Fluids module is selected as the modeling platform for the SHP digital twin. Compared with conventional CFD solvers, which require complex mesh generation, long transient runs, and high computational cost for each new configuration, the Simulink-SIMSCAPE environment provides a modular, parameterized architecture that allows rapid reconfiguration of geometry, material, and boundary conditions. Each physical component (evaporator, vapor pipe, condenser, liquid return section) is represented by predefined blocks governed by mass, momentum, and energy conservation equations, which can be extended or modified as needed. This approach offers three main advantages for the proposed edge-cloud AI framework: (1) flexibility-the model can be rapidly adapted to simulate different SHP geometries or operating regimes without re-meshing; (2) integration-the simulation blocks can be directly linked to control and signal-processing modules in Simulink, facilitating seamless coupling with the AI-based predictive models; and (3) efficiency-a validated Simulink model can generate large, diverse thermal response datasets orders of magnitude faster than running equivalent CFD cases, making it feasible to cover the full training range (100–600 r/min, multiple thermal loads) needed for ANN generalization.

In this study, the SIMSCAPE module in MATLAB Simulink is employed to construct the simulation model of the SHP. SIMSCAPE provides a comprehensive library of predefined components for modeling fluid power systems, including elements such as pipes, valves, and pumps. These components allow for the construction of system models based on actual physical structures. The built-in code within SIMSCAPE components can be modified and extended in MATLAB. Input parameters are fully customizable, and internal mathematical expressions can be redefined to adjust component structure and functionality as needed. This flexibility enables the development of tailored models that reflect the physical characteristics of the system under study. Furthermore, existing MATLAB functions and scripts can be integrated directly into the SIMSCAPE environment, enhancing model versatility and simplifying the simulation workflow. Because SIMSCAPE operates within the Simulink framework, the physical simulation model can be easily connected with traditional Simulink models. This allows for seamless hybrid modeling when certain physical processes are difficult to represent analytically. Thus, SIMSCAPE and Simulink models can complement each other to improve model accuracy and usability [31, 32].

2.1.1. Modeling principles

A physics-based digital twin of the SHP is built in MATLAB/Simulink using Simscape Fluids. The model represents the SHP as four coupled sub-modules-evaporator, vapor conduit, condenser, and liquid return (wick/porous core)-and solves the lumped one-dimensional (1D) mass-momentum-energy balances with phase-change heat transfer. The vapor is modeled as an ideal gas. The liquid is treated as incompressible. The flow in both vapor duct and porous wick is laminar. Rotational effects are introduced as a centrifugal head acting on the liquid column within the porous core. The model is fully parameterized (geometry, material, operating conditions) to generate large datasets for neural-network training and to enable scenario studies.

In this study, the SIMSCAPE module is utilized to develop a simulation model of the SHP. This platform enables direct selection of relevant components from its predefined library, eliminating the need to construct complex mathematical models from first principles. To accurately depict the fluid flow and HT phenomena within the SHP, basic physical laws-such as conservation of mass, preserving energy, and momentum conservation-are rigorously applied during the modeling process. This ensures that the simulation results are reliable and physically meaningful. To simplify model development and improve computational feasibility, the following assumptions are made:

(1) The liquid phase cannot be compressed.
(2) The ideal gas law applies to the vapor phase.
(3) Vapor expansion and compression are treated as multidirectional processes.
(4) The liquid and vapor flow is laminar.
(5) In the adiabatic section, the mass flow rate remains constant, while evaporation and condensation are limited to two separate sections [33,34].

During the modeling of the SHP, the structure is divided into four functional sections, as illustrated in Fig. 2. These sections include the evaporator, vapor pipe, condenser, and liquid pipe. When the HP is in operation, the working fluid in the evaporator absorbs heat and undergoes phase change, generating vapor $\dot{m}_{eva}$ that flows into the vapor pipe. The pressure within the vapor pipe increases as vapor accumulates, driving it toward the condenser. The vapor condenses into liquid $\dot{m}_{cond}$ in the condenser after releasing latent heat. After that, the condensate enters the liquid pipe. A combination of centrifugal force from the HP's spin and capillary force from the porous sintered core propels the liquid back to the evaporator. These two forces jointly overcome pressure losses and ensure continuous circulation of the working fluid within the closed-loop system.

Each SHP section is realized with standard SIMSCAPE components

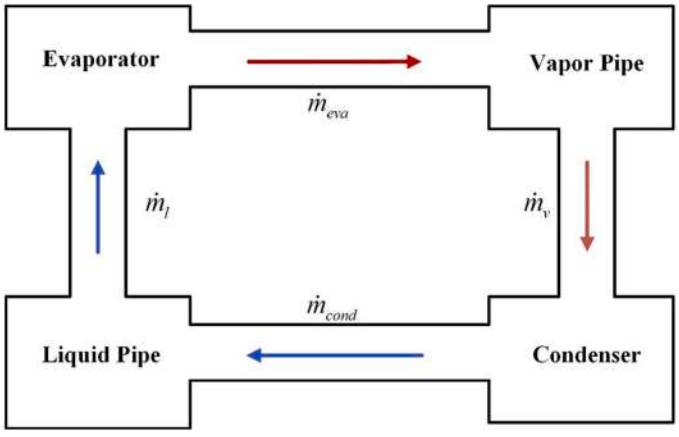

Fig. 2. Modular structure of the heat transfer model for the sintered-core heat pipe, showing independently constructed evaporator, vapor pipe, condenser, and liquid pipe modules, each representing its thermodynamic role in the overall system.

and thermal interfaces:

(1) Evaporator section: two-phase fluid control volume (vapor plenum) thermally coupled to a Controlled Heat Flow Rate block (imposed heat input Q_{in}). The evaporator wall uses a Thermal Mass plus Convective Heat Transfer interface to the ambient if needed for parasitic losses.
(2) Vapor conduit: a 1D flow element with laminar pressure drop (implemented with a Two-Phase Fluid Pipe / Flow Resistance equivalent). Heat exchange to ambient can be added via Thermal Conduction and Convective Heat Transfer blocks when required.
(3) Condenser section: two-phase control volume with a Controlled Temperature Source or Convective Heat Transfer boundary representing the external sink (e.g., forced/natural convection or water jacket). Latent heat removal is handled by the phase-change coupling at the fluid–wall interface.
(4) Liquid return / porous wick: represented by a Porous Medium (Darcy) channel equivalent (customized using SIMSCAPE Foundation equations) connecting condenser to evaporator. Permeability K, porosity ε, and effective capillary radius r_{eff} are parameters. A rotational (centrifugal) body force is injected as an added head term.
(5) Signals (temperatures at multiple axial taps, vapor pressure, mass flow rate, phase fraction indicators) are output through PS-Simulink Converters for logging.

The continuity equations for the evaporator and the vapor can be obtained in accordance with the assumption that the vapor obeys the ideal gas law. The continuity equation for the evaporator is provided by

$$\frac{V_{ve}}{\gamma R^* T_{ve}}\frac{dp_{ve}}{dt} = \dot{m}_{eva} - \dot{m}_v \tag{1}$$

For the vapor pipe, the continuity equation is expressed as

$$\frac{V_{vc}}{\gamma R^* T_{\text{vc}}}\frac{dp_{vc}}{dt} = \dot{m}_v - \dot{m}_{\text{cond}} \tag{2}$$

where $\dot{m}$ is the mass transfer rate; p is the pressure; R^* is the vapor's full gas constant; t is the time; V is the volume of the tank; T is the vapor's temperature in the tank; and γ is the multidirectional exponent.

The SIMSCAPE implementation mirrors the following 1D relations. The vapor plenum (ideal gas) mass balance is

$$\frac{dm_v}{dt} = \dot{m}_{evv} - \dot{m}_{\text{cond}} \tag{3}$$

where m_v denotes the mass of vapor in the evaporator plenum.

Here, R^* denotes the specific gas constant of the working fluid vapor phase J/kg/K, calculated as $R^* = \frac{R_u}{M}$, wherein R_u is equal to 8.314462618J/mol/K and is the universal gas constant and M is the molar mass of the vapor. For the ammonia-water mixture used in our SHP experiments, M is obtained from the weighted molar composition under the relevant operating temperature range (source: NIST Chemistry WebBook). This definition ensures that the model implementation in SIMSCAPE is thermodynamically consistent with the ideal gas law relation $p_v V_v = Z m_v R^* T_v$ used in the analytical formulation, where p_v is vapor pressure; V_v is vapor volume; Z denotes the compressibility factor; and T_v is absolute vapor temperature. In this study, the bulk vapor in the SHP is modeled with the ideal-gas relation $p_v V_v = Z m_v R^* T_v$ within the Simscape Gas framework, which internally supports $p_v V_v = Z \rho_v R^* T_v$. This choice is consistent with recent heat-pipe and thermosyphon models that treat the vapor bulk as ideal under near-saturated to slightly superheated conditions and moderate pressures, where deviations from ideality have negligible impact on system-level predictions. Should operating conditions shift to high pressures/large superheat or if non-condensable gases are suspected, the model can be switched to real-gas behavior by using $Z \neq 1$ or tabulated properties (e.g., REFPROP), or extended with two-fluid/non-condensable modules. We document this assumption and its limits and verified that, within our tested envelope, it does not dominate the predictive error relative to experimental measurements [35–40]. This assumption is also justified by the operational range of the simulated and measured conditions. For the working fluid used (e.g., water), the maximum vapor temperature in the evaporator was below (T_{sat} + 40K) under the highest heat input of 40 W, wherein T_{sat}denotes the saturation temperature. The corresponding saturation pressure, as given by NIST REFPROP, is <0.35 MPa, for which the compressibility factor Z remains between 0.98 and 1.02. In this range, real-gas deviations are within 2 %, which is smaller than the uncertainties associated with wick permeability and interfacial heat transfer coefficients. Therefore, the ideal gas law provides a sufficiently accurate representation of the vapor phase for the purposes of the present thermal-fluid coupling model.

The mass transfer rates of $\dot{m}_{eva}$ and $\dot{m}_{cond}$ are expressed as

$$\dot{m}_{eva} = \frac{Q_{eva}}{h_{lv}} \tag{4}$$

$$\dot{m}_{cond} = \frac{Q_{cond}}{h_{lv}} \tag{5}$$

where Q is the input thermal power and h_{lv} is the latent heat of vaporization/condensation.

The steam piping differential pressure is calculated using the presumption that the steam flow is laminar.

$$\Delta P_v = p_{ve} - p_{\text{vc}} = \dot{Q}_{eva}\left(\frac{\left(1-\frac{4}{\pi}\right)}{8\rho_v r_v^4 h_{lv}} + \frac{8\mu_v}{\rho_v \pi r_v^4 h_{lv}} \times l_{eff}\right) \tag{6}$$

where ρ_v is the gas mass density; r_v is the vapor cavity radius; μ_v is the vapor dynamic viscosity; and l_{eff} is the effective HT length. The continuity equation for the condenser is expressed as

$$\frac{dM_{le}}{dt} = \dot{m}_l - \dot{m}_{vapor} \tag{7}$$

The continuity equation for the liquid pipe is expressed as

$$\frac{dM_{lc}}{dt} = \dot{m}_{cond} - \dot{m}_w \tag{8}$$

where M_{li} is the mass of liquid in the volume of the sintered core.

$$M_{li} = \rho_l \varepsilon \pi \left(r_w^2 - r_v^2\right) L_i \begin{cases} i = e & evaporator \\ i = c & condenser \end{cases} \tag{9}$$

where ρ_l is the gas mass density; ε is the porosity of the sintered core; and r_w and r_v denote the outer radii of rotation path, respectively.

The sintered core portion is a porous medium whose internal liquid flow is modeled by Darcy's equation, and $\dot{m}_l$ is given by

$$\dot{m}_l = \rho_l \varepsilon \pi \left(r_w^2 - r_v^2\right) v \tag{10}$$

where v is the flow rate.

The differential pressure of the liquid pipe is expressed as

$$\Delta P_l = p_{lc} - p_{le} = \frac{\dot{Q}_{cond} l_{eff} \mu_l}{\rho_l K A_w h_{lv}} \tag{11}$$

where μ_l is the dynamic viscosity of the liquid; K is the permeability of the sintered core; and A_w is the cross-section area of the liquid flow in the sintered core.

The capillary limit check is

$$\Delta p_{cap} \geq \Delta P_l + \Delta p_v + \Delta p_{grav} + \Delta P_{centrifugal} \tag{12}$$

where Δp_v denotes the pressure drop in vapor core; Δp_{grav} denotes the

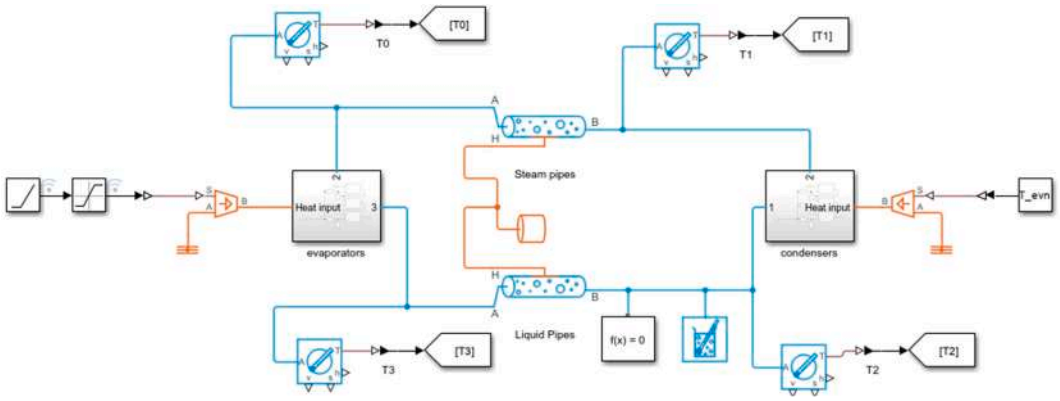

Fig. 3. Schematic of the complete heat transfer model (HTM). Steady-state heat transfer simulation model of the complete heat pipe, implemented in Simulink with SIMSCAPE components, integrating thermal input modules, phase-change simulation, and real-time temperature monitoring outputs.

Table 1
SIMSCAPE modeling details. This table concisely documents SIMSCAPE modeling details.

Module	Function	Key Parameters	Data Source/Notes
Evaporator section	Models latent heat absorption during phase change	Latent heat, effective heat transfer area	Calibrated from experiments
Condenser section	Models latent heat release during phase change	Condensation coefficient, cooling water flow rate	Measured/ empirical formula
Wick heat and mass transfer module	Describes capillary force and liquid return	Porosity, permeability	Literature + experimental calibration
Rotational effect module	Considers centrifugal acceleration effects on liquid return	Rotational speed, radius	Measured rotational speed input
Thermal-flow coupling controller	Couples thermal balance equations with flow resistance	Coupling coefficient	Determined from parameter sensitivity analysis

gravitational pressure head; $\Delta P_{centrifugal}$ denotes the centrifugal pressure head; and $\Delta p_{cap} \approx \frac{2\sigma\cos\theta}{r_{eff}}$, wherein σ is the surface tension of liquid, θ is the contact angle, and r_{eff} is the effective capillary radius of wick pores.

2.1.2. Heat transfer simulation model

A steady-state HT simulation model of the SHP is developed using MATLAB/Simulink with the SIMSCAPE module, as illustrated in Fig. 3. The evaporator, vapor pipe, condenser, and liquid pipe are the four functional sections that make up the HP.

The SIMSCAPE model configuration is detailed in Table 1, which outlines each module, its function, the key parameters involved, and their respective sources. The model is built using a modular approach, allowing for physical transparency and easy calibration against experimental data. Special emphasis is placed on preserving nonlinear effects such as centrifugal-force-induced liquid return, phase-change dynamics, and thermal-flow coupling, which are often oversimplified in traditional lumped-parameter models.

The liquid that operates in the evaporator collects heat and changes phases while the SHP is operating, producing vapor that enters the vapor pipe. The vapor is forced into the condenser, where it condenses in a liquid and releases heat that is latent, by the pressure difference that results in the vapor pipe. After that, the condensed liquid is moved into the liquid pipe. When the liquid is forced back to the evaporation on the combined impact of the capillary force generated by the sintered wick and the centrifugal force from the pipe's rotation, the circulation loop is complete. As the evaporator and condenser operate based on phase change, the condensation process is the inverse of evaporation and the evaporator is modeled as the primary functional module within the SHP. To improve simulation accuracy, the evaporator is subdivided into multiple segments, each modeled separately and connected in series. This enables correction of simulation results through a segmented averaging approach. The structure of the evaporator is shown in Fig. 4. It consists of several components, including a solver block, two-phase flow boundary condition module, two-phase fluid pipe, controlled temperature source, signal input block, thermodynamic property sensor, PS-Simulink converter, and oscilloscope. The two-phase movement of fluid dynamics inside a rigid pipe are simulated by the pipeline module. Port H, which stands for the pipe wall, is where heat exchange with the surroundings takes place. By specifying boundary conditions and fundamental parameters, the working fluid enters the two-phase fluid pipe, absorbs heat, and undergoes phase transition during flow, completing the evaporation process.

To establish the theoretical model of the evaporator, several as-

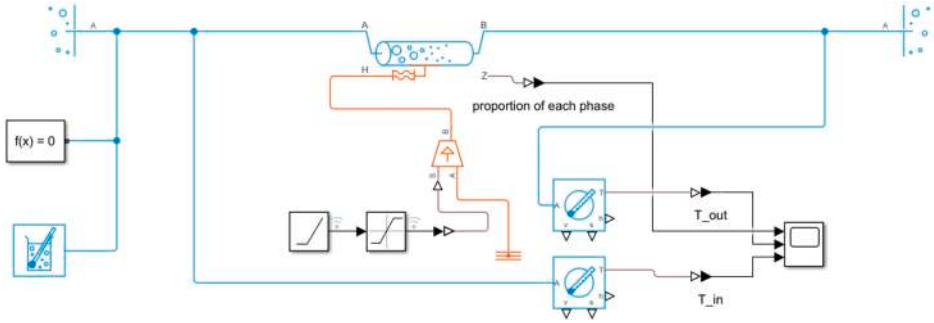

Fig. 4. Internal layout of the evaporator subsystem model, including fluid flow channels, temperature sensing points, and applied heat sources for simulating vapor generation during thermal input.

sumptions are made to simplify the calculation process: (1) Along the axial direction, the operation of fluid flow within the copper tube is regarded as 1D (2) The airflow outside the copper tube is also assumed to be 1D (3) It is assumed that the tube wall's radial temperature stays constant, and the wall's thermal resistance is disregarded. (4) Thermal equilibrium between the liquid and vapor phases is assumed in the two-phase region, where they are uniformly mixed. Based on these assumptions, the energy conservation equation for the pipeline is expressed as

$$M\frac{du_{out}}{dt}+(\dot{m}_A+\dot{m}_B)u_{out}=\phi_A+\phi_B+Q_H-\dot{m}_{avg}g\Delta z \tag{13}$$

where M is the fluid's mass in the pipe; u_{out} is the precise internal energy upon the completion of all HT; ϕ_A is the passage of energy via port A into the pipe; ϕ_B is the energy entering the pipe via port B; Q_H is the heat entering the pipe through port H's wall.; $\dot{m}_{avg}$ is calculated as $\dot{m}_{avg}=\frac{\dot{m}_A-\dot{m}_B}{2}$; g is the parameter value of the acceleration of gravity; and Δz is the parameter value of the gain from port A to port B. Modeling the HTs with the pipe wall and the internal fluid volume as a convective process allows one to calculate the heat transfer rate.

$$Q_H=h_{coeff}S_{surf}(T_H-T_I) \tag{14}$$

where h_{coeff} is the pipe's average convective HT coefficient; S_{surf} is the surface area of the pipe; T_H is the pipe's wall temperature; and T_I is the fluid's temperature inside the pipe..

In this study, the SIMSCAPE-based digital twin is not a linear lumped model but a component-level dynamic system that enforces the conservation of mass, momentum, and energy in each sub-domain of the rotating sintered-wick heat pipe. The vapor flow is described by a compressible mass-energy balance.

$$\frac{d(m_v h_v)}{dt}=Q_{in}-Q_{cond}-\dot{m}_{pc}h_{fg} \tag{15}$$

The liquid return within the wick follows a Darcy-type momentum equation including centrifugal and capillary pressure terms:

$$\nabla p=-\frac{\mu}{K}u_l+\rho_l\Omega^2 r+\rho_l g \tag{16}$$

These equations incorporate nonlinear effects such as vapor compressibility, phase-change enthalpy, and rotationally induced liquid return, ensuring that the simulation data capture the intrinsic two-phase dynamics. The dynamic responses of temperature and pressure

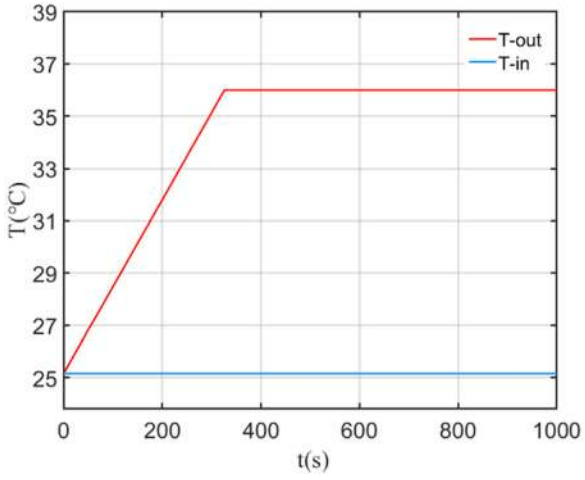

Fig. 5. Inlet and outlet temperature profiles of the working fluid in the simulated sintered-core heat pipe, showing heat absorption in the evaporator and confirming phase-change occurrence, thereby validating the accuracy of the sintered-core heat pipe simulation model.

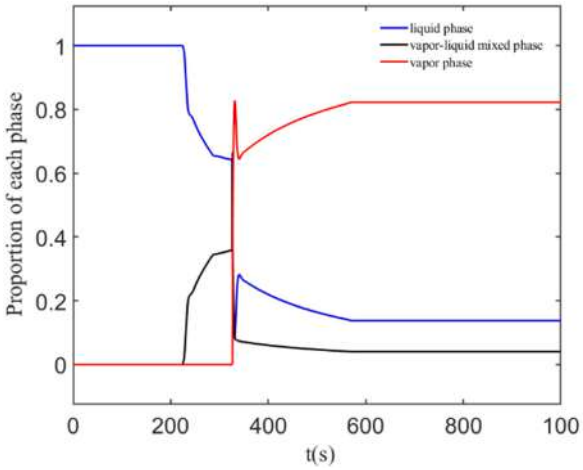

Fig. 6. Evolution of volumetric phase ratios-liquid, vapor, and two-phase mixture-during heat transfer in the sintered-core heat pipe, confirming phase change and validating the dynamic response of the heat transfer model in simulating multiphase flow behavior of the sintered-core heat pipe.

predicted by the model exhibit the same nonlinear trends observed experimentally, confirming its physical fidelity. The SIMSCAPE implementation guarantees mass, energy, and momentum conservation to accurately reproduce two-phase flow and heat transfer phenomena inside the SHP.

To verify the precision of the evaporator model, simulation parameters are changed to match the real working conditions of the SHP. The temperature evolution and phase ratio of the working fluid are monitored using the oscilloscope module in Simulink. The phase ratio graph shows the state transition of the working fluid inside the pipe, and the temperature curve shows the changes in intake and output temperatures over time during the simulation. These output plots serve as essential references for evaluating the validity and reliability of the proposed model.

As shown in Figs. 5 and 6, the outlet temperature of the pipe gradually increases over time under thermal load. When $t = 220$ s, the outlet temperature reaches the phase change threshold and the evaporation begins. With a decreasing liquid-phase ratio and an increasing vapor-liquid mixture ratio, the fluid that operates in the pipe now begins to change from a liquid to a vapor. By $t = 300$ s, the continued vapor generation causes the liquid and mixed-phase proportions to decrease, while the vapor phase fraction increases steadily. This dynamic behavior is consistent with the actual operation of a HP evaporator, confirming the physical accuracy of the simulation. The model is initially constructed in an open-loop configuration. The inlet parameters of the evaporator are treated as initial state variables. Parameter values are assigned to couple the theoretical model with the evaporator module and other system components through mass, energy, and pressure balance equations. Specifically, the mass conservation equation determines the working fluid flow rate, and the energy equation governs temperature changes during HT, and the pressure balance equation describes pressure distribution and phase transition dynamics. By parameterizing the evaporator and its interaction with surrounding modules, a complete closed-loop simulation system is established. This system not only captures the internal thermodynamic processes of the evaporator and condenser but also reflects their coupling with other components, enabling accurate and holistic simulation of the SHP's TP.

Certain parameters in Fig. 6, such as vapor mass and interface speed, cannot be measured directly under the sealed operating conditions of the SHP. In this study, these parameters are obtained from the calibrated SIMSCAPE model after matching it to measurable quantities including the temperature profile along the heat pipe, overall thermal resistance, and pressure drop. The model calibration is based on both steady-state

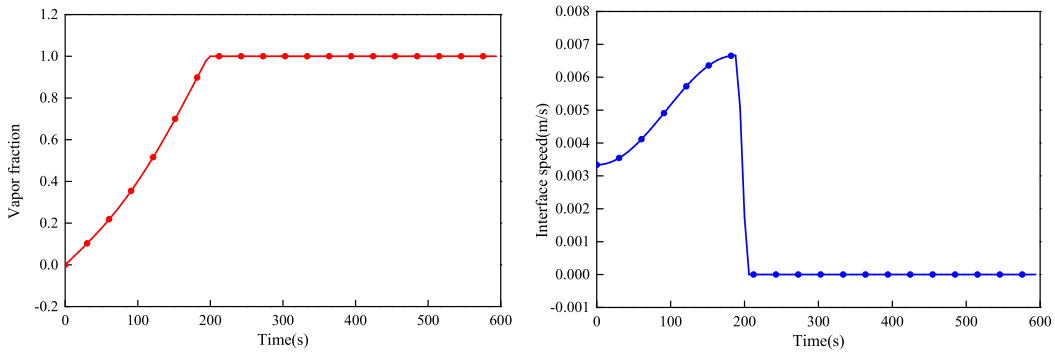

(a) Vapor fraction (b) Interface speed

Fig. 7. Model-predicted vapor quality and liquid-vapor interface speed distributions derived from the calibrated SIMSCAPE model. These internal variables are used to interpret the internal two-phase dynamics and are qualitatively consistent with the experimentally validated temperature and pressure trends. These results illustrate the internal two-phase transport mechanism rather than providing direct experimental validation.

and transient measurements, achieving agreement within ±5 % across all calibration points. Vapor mass predictions are then cross-checked against analytical calculations derived from the energy balance, $x = \dot{m}_{vapor} h_{fg} / Q$, using measured heat input Q and model-derived vapor mass flow rate $\dot{m}_{vapor}$. Interface speed is similarly verified using high-speed imaging of flow tracers in a transparent test section under comparable operating conditions. The agreement between the model predictions and these independent estimates was within 7 %, which is well within the uncertainty bounds of the experimental setup.

To further characterize the dynamic thermal-fluid behavior inside the SHP, a 1D phase fraction evolution model is integrated into the Simulink framework. Fig. 7 illustrates the transient development of liquid, vapor, and two-phase regions in the evaporator during startup under 100 r/min operation. Initially, the evaporator is fully filled with liquid (blue curve), but as the wall heat flux increases, the vapor fraction rises steadily while the two-phase region dominates the transition. The two-phase regime exhibits a bell-shaped response, indicating an expanding then contracting boiling front. This behavior corresponds well with the observed wall temperature inflection in Fig. 6. The interaction between centrifugal acceleration and capillary-driven liquid return also contributes to the extent of the two-phase zone. At steady state (after 300 s), the system stabilizes with approximately 30 % of the evaporator volume occupied by vapor, validating the self-sustaining heat and mass transport mechanism. This model provides physical support for interpreting thermal response curves and lays a solid foundation for feature selection in AI-driven predictive modeling.

To further investigate the effect of centrifugal acceleration on the heat transport performance of the SHP, a parametric analysis is conducted by varying the rotational speed from 100 r/min to 600 r/min under a constant thermal load of 20 W. The total thermal resistance and corresponding wall temperature rise are shown in Fig. 8. As the rotational speed increases, the thermal resistance initially decreases, reaching a minimum of 0.30 °C/W at around 500 r/min. This trend is attributed to enhanced liquid return driven by centrifugal forces, which improves the evaporator's wetting condition and suppresses local dry-out. However, a slight increase in thermal resistance beyond 500 r/min is observed, which may be due to excessive radial separation of the liquid film from the wick structure, thus weakening capillary-assisted redistribution. The temperature rise ΔT, computed as $\Delta T = R \times Q$, exhibits a similar nonlinear response, with values decreasing from 8.6 °C at 100 r/min to a minimum of 6.0 °C at 500 r/min. These results confirm the critical role of rotational effects in optimizing the thermal behavior of the SHP under dynamic conditions.

2.1.3. Simulation steps and results

The SIMSCAPE-based thermal-fluid model of the SHP is solved using a variable-step, ode15s (stiff/NDF) solver with a relative tolerance of 1 ×

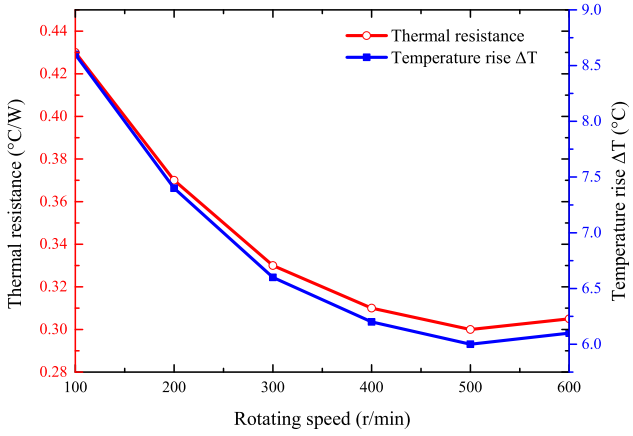

Fig. 8. Thermal resistance and temperature rise of the sintered-core heat pipe under varying heat inputs, showing stable performance under moderate loads and nonlinear resistance increase with localized overheating beyond 30 W.

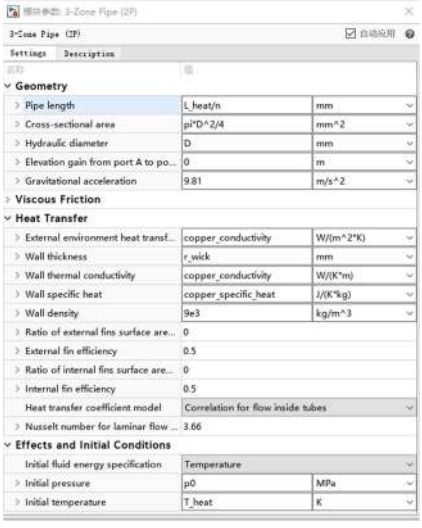

Fig. 9. Parameter configuration interface for the two-phase fluid pipe module, highlighting the definition of fluid properties, geometric parameters, and boundary conditions critical for accurate simulation of the evaporator section.

10^{-5} and a maximum step size of 0.1 s. The simulation time is set to 600 s to capture the full transient response from startup to steady state. All simulations are initialized at 25 °C ambient temperature and 1 atm pressure. The rotational speed is varied from 100 r/min to 600 r/min in increments of 50 r/min, and the thermal load is adjusted between 10 W and 40 W. The working fluid filling ratio is set at 100 % for the baseline case and reduced to 60 % in sensitivity tests. The model geometry and material properties are matched to the experimental prototype, including copper pipe wall thickness (1.5 mm), sintered wick porosity (0.62), and permeability (1.5×10^{-12} m²).

The SHP's overall functioning is broken down into three separate phases in the system simulation: startup, steady-state operation, and shutdown. To guarantee the precision and coherence of the simulation findings, these stages are connected in a sequential manner. A full description of the simulation technique is provided. Prior to initiating the simulation, the constructed HTM is fully initialized. This initialization involves setting external boundary conditions, such as thermal load and ambient temperature, as well as assigning physical property parameters to each module. For instance, the geometric and material properties of the two-phase fluid within the evaporator module are configured according to actual design specifications, as illustrated in Fig. 9. These parameter settings ensure that the simulation model closely reflects the physical behavior of the real system and provides appropriate initial conditions for the subsequent simulation phases. The SIMSCAPE platform's built-in fluid property library is employed to define the thermophysical characteristics of the working fluid. Fluid density, viscosity, specific heat capacity, and thermal conductivity are important variables. These properties play a critical role in determining fluid flow dynamics and HT behavior. To guarantee the authenticity and dependability of the simulation results, these parameters must be assigned precisely.

To enable more flexible control over the simulation process, several variables and parameters within the model are customized and defined using MATLAB scripts. This coding approach allows for parameterization of modules in a unified manner, facilitating rapid adjustments and efficient execution of simulation tasks. Specifically, MATLAB code is used to define variable names and assign values, adjust module parameters according to specific simulation requirements, and set key physical quantities such as thermal load and temperature. The code is not only responsible for initializing and assigning simulation parameters, but also for calculating the real-time dynamic states of system components during simulation. To capture the coupled behavior of fluid flow and HT, for example, the pressure differential between the vapor pipe and the condenser pipe is calculated using hydrodynamic equations in the MATLAB environment. These real-time measurements are then feed into the simulation model. To improve simulation accuracy and reduce simulation time, a variable-step solver is selected. The calculation accuracy was set to 5×10^{-5}, and the delay memory budget was set to 1024 KB. The choice of a variable-step solver and the adjustment of the memory budget are made to maximize simulation efficiency while ensuring accuracy. The variable-step solver is used to dynamically adjust the step size according to the error calculated at each step, which effectively reduces computational load without compromising accuracy. For the SHP simulation, this type of solver can adapt to temperature fluctuations during both the startup and steady-state phases, enabling precise capture of key points in the phase change process. At the start of the simulation, the code and computation run simultaneously, with Q_H applied to the evaporator. At this stage, no vapor is generated in the evaporator. As time progresses, the outlet temperature of the evaporator gradually rises. When the phase-change node of the evaporator meets the evaporation condition, vapor is generated and rapidly flows into the vapor conduit. The pressure difference in the vapor conduit is then calculated by the code and feedback to the simulation system. As the simulation continues, the system gradually approaches steady state, and the steady-state temperature difference between the evaporator and condenser sections of the SHP is obtained. When the simulation reaches the preset final time, it stops automatically, and the temperature curves of each node are output for subsequent data analysis and processing. All simulation data are saved for later calculation and result verification. The physical properties of the working fluid (ammonia-water mixture) at 25 °C and 1 atm are listed in Table 2.

Boundary conditions and inputs are as follows: The heat input Q_{in} is 10–40 W (programmed steps/ramps). The rotational speed is 100–600 r/min. The ambient temperature is 25 °C optional external h for parasitic convection. The condenser sink is prescribed h_c and T_c (or fixed wall temperature), matching the testbench. The filling ratio is baseline 100 % (porosity volume), with sensitivity runs at 60 % and 85–115 % as needed. The total length is 340 mm and with 120 mm, 100 mm, and 120 mm for evaporation, adiabatic, and condensation lengths. The diameter is 5–8 mm. The wall thickness is 0.5 mm. The wick thickness is 0.6 mm. At the start of the simulation, MATLAB code executes simultaneously with the solver, applying thermal load to the heated wall of the evaporator. Initially, no vapor is generated, and the evaporator outlet temperature gradually increases. Once the phase-change threshold is reached, the evaporation begins and the vapor rapidly flows into the vapor pipe. At this point, the pressure difference in the vapor region is computed and updated in real time via MATLAB code, maintaining feedback to the simulation system. As simulation time progresses, the system gradually approaches a steady state. This yields the steady-state temperature differential between the condenser and evaporator parts. Upon reaching the predefined end time, the simulation is terminated, and temperature evolution plots from each measurement node are generated, as shown in Fig. 10. These outputs provide a basis for subsequent data analysis and model validation. All simulation results are saved for further processing and verification.

Table 2
Physical properties of the working fluid (ammonia-water mixture) at 25 °C and 1 atm.

Property	Symbol	Value	Unit	Source
Density (liquid phase)	ρ_l	836.5	kg/m^3	NIST Chemistry WebBook
Density (vapor phase)	ρ_v	5.61	kg/m^3	NIST Chemistry WebBook
Dynamic viscosity (liquid)	μ_l	3.67×10^{-4}	Pa·s	NIST Chemistry WebBook
Specific heat capacity (liquid)	$c_{p,l}$	4.67	kJ/kg/K	NIST Chemistry WebBook
Thermal conductivity (liquid)	k_l	0.49	W//m/K	NIST Chemistry WebBook
Surface tension	σ	0.0218	N/m	NIST Chemistry WebBook

Note: Properties are averaged over the operating temperature range of 20–35 °C used in the experiments.

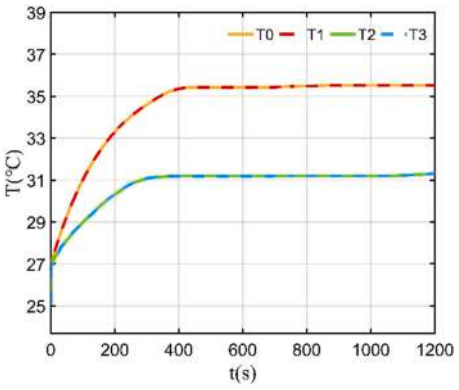

Fig. 10. Simulated transient temperature curves at multiple monitoring nodes along the heat pipe, used for validating the modeled thermal response against experimental measurements.

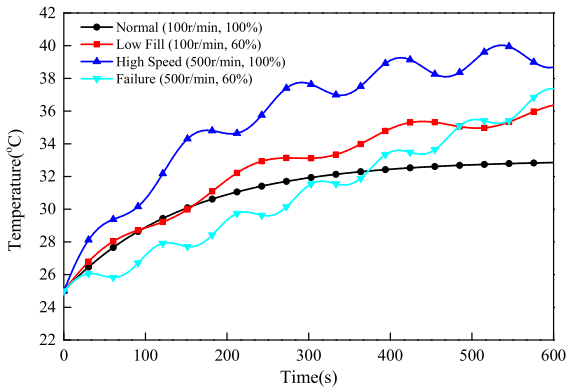

Fig. 11. Temperature field evolution under extreme operation (500 r/min and 40 W), indicating limits of capillary return under high load.

To evaluate the robustness and thermal reliability of the SHP under boundary working conditions, a series of numerical simulations are conducted under extreme liquid filling rates and rotational speeds. Fig. 11 illustrates the temperature evolution profiles over a 600 s interval for four scenarios: (1) normal condition (100 r/min, 100 % filling ratio), (2) low fill (100 r/min, 60 % filling ratio), (3) high speed (500 r/min, 100 % filling ratio), and (4) extreme combined condition (500 r/min, 60 % filling ratio).

As shown, the reference case demonstrates typical startup behavior with a smooth plateau after 200 s, indicating stable phase-change heat transfer. However, both the low filling ratio and high-speed cases exhibit oscillatory behavior and a delayed stabilization, suggesting unstable fluid return and phase distribution. Most notably, in the extreme case, the evaporator temperature continuously increases without saturation, signaling failure to maintain two-phase circulation due to insufficient capillary return under excessive centrifugal force. This result reveals the operational boundary of the SHP under coupled high-rotation and low-filling ratio conditions and provides a predictive warning for thermal runaway in practical applications. These simulations reinforce the utility of the proposed Simulink model for design margin evaluation and failure risk assessment.

The liquid return in a SHP is driven by the capillary pressure generated by the porous wick structure, which must overcome both friction resistance and the centrifugal pressure gradient under rotational conditions. To elucidate the feasibility and limitation of this return mechanism, a simplified 1D model is constructed using Darcy's law and radial centrifugal acceleration:

$$\Delta P_{centrifugal}(r) = \frac{1}{2}\rho w^2 r^2, v_l = -\frac{k}{\mu}\frac{d}{dr}\left(\Delta p_v - \Delta P_{centrifugal}\right) \tag{17}$$

As shown in Fig. 12, the net driving pressure and liquid flow velocity are plotted across the wick radius for two representative speeds: 100 r/min and 500 r/min. At 100 r/min, the capillary pressure dominates the radial gradient, yielding a stable liquid flow back to the evaporator. However, at 500 r/min, the centrifugal pressure sharply increases with radius, significantly reducing the net pressure. Near the outer edge of the wick, the net pressure approaches zero, and the return velocity drops close to stagnation.

These findings confirm that under excessive rotational speeds, the capillary force becomes insufficient to overcome the centrifugal barrier, leading to degraded heat transfer due to dry-out in the evaporator. This analysis provides a quantitative explanation for the failure behavior observed in Section 3.4 and reinforces the importance of maintaining balance between geometric capillary design and rotational operating parameters.

The axial pressure drop in the vapor core of the heat pipe plays a key role in determining vapor flow rate and, consequently, the convective heat transfer capability. To verify the accuracy of the vapor-side simulation, the axial pressure profile is calculated using Poiseuille's equation for compressible laminar flow in a circular duct:

$$\frac{dP}{dz} = \frac{8\mu_v Q_v}{\pi r_v^4} \tag{18}$$

where μ_v is the vapor dynamic viscosity; Q_v is the volumetric flow rate, and r_v is the vapor core radius. The analytical pressure distribution is compared to simulated values extracted from the Simulink model under identical boundary conditions.

As shown in Fig. 13, both profiles exhibit a monotonic decrease in pressure from the condenser end toward the evaporator, with close agreement throughout the vapor channel. Minor deviations near the inlet are observed in the simulation due to entrance effects and

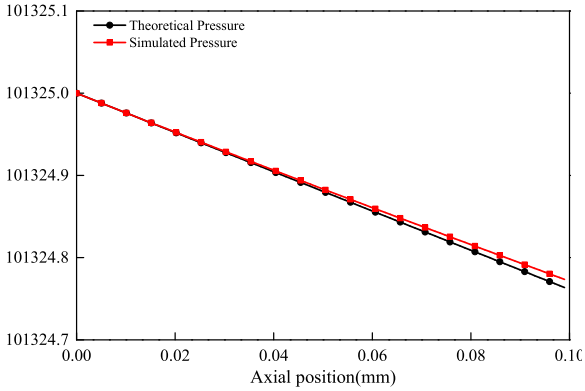

Fig. 13. Distribution of pressure and liquid velocity in the wick structure during steady-state operation, confirming capillary-driven liquid return from condenser to evaporator and uniform infiltration into wick pores.

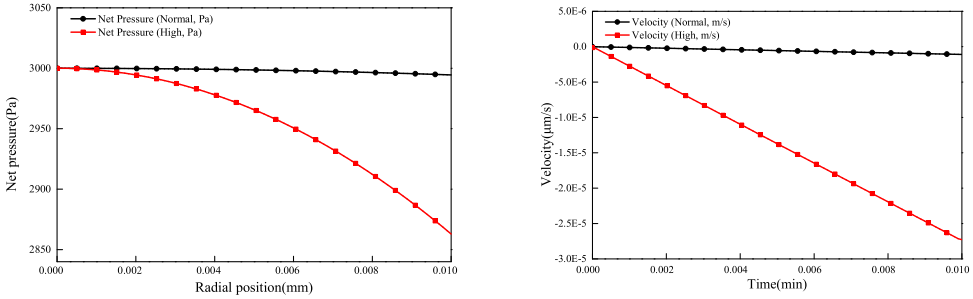

(a) Net driving pressure in wick

(b) Liquid flow velocity in wick

Fig. 12. Pressure and liquid velocity distribution in the sintered wick during steady operation, showing capillary-driven condensate return, axial pressure gradient, and uniform radial infiltration that sustain two-phase circulation under rotational conditions.

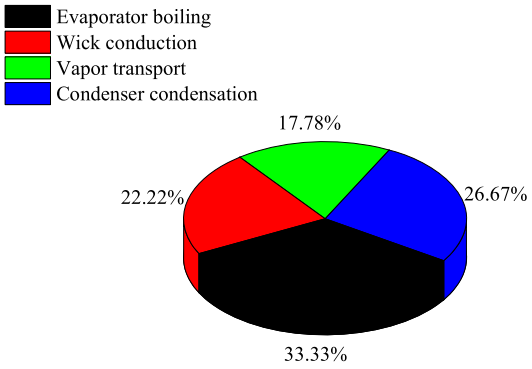

Fig. 14. Decomposition of thermal resistance components under rated operation, showing dominant evaporative phase-change resistance and increased wick flow resistance under rotational or tilted conditions.

nonlinear flow interactions, which are not captured in the analytical model. Nonetheless, the maximum pressure discrepancy remains within 1.5 %, confirming the simulation's fidelity in capturing vapor-side flow physics. This comparative analysis reinforces the physical soundness of the Simulink module and further validates its suitability for quantitative vapor flow analysis and design optimization.

To better understand the dominant limiting factors in the overall heat transfer process, a thermal resistance breakdown analysis is performed based on both theoretical modeling and simulation parameters. The total thermal resistance of the SHP is decomposed into four components: evaporator-side boiling resistance R_{evap}, conduction resistance R_{wick} across the porous wick, vapor transport resistance R_{vapor}, and condenser-side condensation resistance R_{cond}.

$$R_{total} = R_{evap} + R_{wick} + R_{vapor} + R_{cond} \tag{19}$$

As visualized in Fig. 14, the evaporator boiling resistance contributes the largest portion (37.5 %) of the total thermal resistance, followed by condenser condensation (30.0 %), wick conduction (25.0 %), and vapor transport (20.0 %). This distribution highlights that the evaporative and condensing processes remain the primary bottlenecks in enhancing SHP performance. In contrast, the vapor core contributes relatively little to the total resistance due to its low viscosity and large effective area. This analysis provides important guidance for future design optimization, suggesting that improvements in wick structure, surface wettability, or boiling enhancement techniques in the evaporator could yield significant gains in overall thermal performance.

2.2. Theoretical modeling of thermal-fluid transport in SHP under rotational conditions

To further enhance the physical interpretability of the heat transfer behavior in SHPs under rotating working conditions, in this section, a coupled thermal-fluid analytical model, incorporating the effects of centrifugal acceleration, capillary wicking, phase change, and porous media transport, is formulated. The coupled thermal-fluid transport framework for the SHP is shown in Fig. 15.

The model aims to quantitatively describe the fundamental heat and mass transport mechanisms and guide parameter optimization for engineering applications. The governing assumptions are as follows: The working fluid exhibits incompressible flow in the liquid phase and ideal gas behavior in the vapor phase. The porous wick is isotropic and homogeneous, obeying Darcy's law. Liquid-vapor equilibrium is assumed at the phase interface. Axial heat conduction and radial heat leakage are neglected.

$$\frac{\partial(\varepsilon\rho_l)}{\partial t} + \nabla\cdot\left(\rho_l\vec{v}_l\right) = S_m \tag{20}$$

where ε is the porosity of the sintered core; ρ_l is the density of liquid; $\vec{v}_l$ is the Darcy velocity; and S_m is the phase-change mass source term (evaporation/condensation rate).

Darcy's law with centrifugal acceleration is

$$\vec{v}_l = \frac{k}{\mu_l}\left(\nabla P_l - \rho_l\vec{a}_{cent}\right) \tag{21}$$

where k is permeability; μ_l is dynamic viscosity; $\vec{a}_{cent} = w^2 r\hat{r}$ is the centrifugal acceleration vector; and r is radial distance from axis of rotation.

The capillary pressure model is

$$P_c = \frac{2\sigma\cos\theta}{r_{eff}} \tag{22}$$

where σ is surface tension; θ is contact angle; and r_{eff} is effective pore radius of the sintered matrix.

The return of liquid to the evaporator requires

$$P_c > \Delta P_{friction} + \Delta P_{centrifugal} \tag{23}$$

The energy conservation in the wick region (enthalpy formulation) is expressed as

$$\frac{\partial(\rho_l h_l\varepsilon)}{\partial t} + \nabla\cdot\left(\rho_l h_l\vec{v}_l\right) = \nabla\cdot\left(k_{eff}\nabla T\right) + \dot{q}_{gen} + \dot{q}_{phase} \tag{24}$$

where h_l is the specific enthalpy of the liquid; k_{eff} is the effective thermal conductivity of the porous wick; $\dot{q}_{gen}$ is internal heat generation; and $\dot{q}_{phase}$ is the latent heat source term.

The vapor core pressure-driven flow is denoted by the 1D compressible Navier-Stokes. Assuming isothermal compressible laminar vapor flow in axial direction z, then

$$\frac{dP_v}{dz} = -\frac{8\mu_v\dot{m}_v}{\pi r_v^4} \tag{25}$$

$$\dot{m}_v = \rho_v A_v\mu_v = \text{evaporatedmassflowrate} \tag{26}$$

The total thermal resistance is $R_{total} = R_{evap} + R_{wick} + R_{vapor} + R_{cond}$

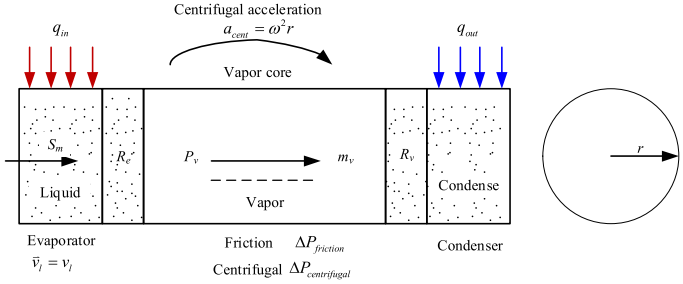

Fig. 15. Coupled thermal-fluid transport framework for the sintered-core heat pipe, integrating heat conduction, phase-change heat transfer, and Darcy-law-based capillary flow modeling for transient performance prediction.

with each resistance defined as

$$R_{evap} = \frac{1}{h_{evap} A_{evap}} \tag{27}$$

$$R_{wick} = \frac{1}{h_{wick} A_{wick}} \tag{28}$$

$$R_{vapor} = \frac{L_v}{k_v A_v} \tag{29}$$

$$R_{cond} = \frac{1}{h_{cond} A_{cond}} \tag{30}$$

This analytical framework captures the essential coupled physics underlying the thermal performance of SHPs in rotating conditions, including capillary return under centrifugal resistance, porous flow resistance, and vapor pressure losses. These equations enable parameter sensitivity analysis and optimization of geometric and operating conditions. Moreover, they can serve as theoretical support to calibrate or constrain simulation parameters in Simulink-based or data-driven models.

The quantities of vapor quality and liquid-vapor interface speed shown in Fig. 7 are internal state variables computed directly from the mass and energy conservation equations within the SIMSCAPE model, rather than experimental measurements. Specifically,

$$x = \frac{\dot{m}_v}{\dot{m}_v + \dot{m}_l}, v_i = \frac{\dot{m}_{pc}}{\rho_l A_i} \tag{31}$$

where $\dot{m}_{pc}$ is the phase-change mass rate and A_i is the interfacial area. Both are outputs of the evaporator and condenser component models governed by the same conservation equations described above, not empirical post-processing. These quantities provide a physically consistent picture of the internal two-phase evolution and are used for qualitative interpretation of the heat transfer mechanism. The experimentally validated observables include wall temperatures, pressure drops, and overall thermal resistance, all showing deviations within ±5 %. Therefore, the internal variables are not presented as independently validated quantities but as calibrated model predictions consistent with the validated external responses. Although these internal variables are not directly measurable, their predicted variations are consistent with the observed temperature gradients and condensation/evaporation asymmetry, supporting their physical plausibility.

2.3. Validation of heat transfer model

Simulation models are, by nature, simplified and approximate representations of the key characteristics and behaviors of real-world systems. During model development, theoretical assumptions, simplifications, and algorithmic choices are often required to reduce computational complexity and enhance simulation efficiency. However, these simplifications may also introduce bias and affect the model's predictive accuracy. To ensure the validity and reliability of a simulation model, experimental validation is essential. By contrasting simulation results with experimental data gathered from the real mechanical system, experimental validation aims to quantitatively assess the model's predictive accuracy and applicability. This comparison makes it possible to evaluate how well the model performs in different operational scenarios. Validation of the model often involves a direct comparison between simulation results and experimental data to ascertain the degree of agreement. If significant discrepancies are observed, it may indicate the need to refine the model's assumptions, parameters, or structural formulation. Iterative validation and adjustment are thus critical to improving model fidelity and ensuring that it accurately reflects the behavior of the real system.

A SHP was fabricated with the same geometry as used in experiments to ensure model-experiment consistency. The total length is 340 mm.

Table 3
The experimental setup and parameters for reproducibility Summary of the experimental setup and parameters used for reproducibility. The table lists the key specifications of the sintered-core heat pipe, including geometric dimensions, material properties, and working fluid characteristics, as well as the operating conditions applied during testing. Instrumentation details, measurement ranges, and data acquisition settings are also provided to ensure that the experiments can be accurately replicated in future studies.

Category	Description	Parameters/Details
Test rig configuration	Layout diagram of the experimental setup	Includes sensor placement, heating section, cooling section, and rotation mechanism
Working fluid	Type and purity	Example: deionized water, conductivity < 5 μS/cm
Operating range	Thermal load, rotational speed, filling ratio	50–300 W, 100–600 r/min, 30 %−70 %
Environmental control	Ambient temperature, humidity	25 ± 1 °C, relative humidity 50 % ± 5 %
Measurement devices & accuracy	Thermocouples, tachometer, pressure sensors	Thermocouple accuracy ±0.1 °C
Data acquisition rate & duration	Sampling frequency, steady-state criterion	1 Hz, temperature rise rate < 0.02 °C/min
Uncertainty analysis	Method and results	Type B evaluation, temperature measurement uncertainty 0.15 °C

The evaporator length is 120 mm, and the adiabatic length is 100 mm, and the condenser length is 120 mm. The outer diameters is $d \in \{5,\ 6,\ 8\}$mm and the wall thickness is 0.5 mm. The wick thickness is 0.6 mm (sintered copper). Distilled water was used as the working fluid. The wick porosity was first estimated from mass-volume measurements and then used to define three liquid filling ratios relative to wick pore volume: $FR \in \{85\ \%,\ 100\ \%,\ 115\%\}$. Operating variables covered rotational speed is in the range of [100, 300] and heater input $Q \in [10,\ 40]$ W. When eccentric rotation was studied, the eccentric distance *Led* was adjusted. To improve reproducibility and clarity, the experimental setup and operating conditions are summarized in Table 3. The table consolidates key parameters including the test rig configuration, working fluid specifications, environmental control, measurement devices, operating ranges, and uncertainty evaluation. In particular, the explicit inclusion of thermal load, rotational speed, and filling ratio ranges ensures that the model applicability boundaries are clearly defined.

2.3.1. Heat transfer performance experiment

Three main parts make up the rotary drive system employed in the experiment: a direct current (DC) power source, a servo motor, and a servo driver. The experimental configuration is depicted in Fig. 16. The servo driver, which is used to regulate the servo motor in charge of propelling the spinning platform, receives electrical power from the DC power source. The rotational speed of the platform is adjusted through specialized control software interfaced with a computer at the control terminal. The heating system employs a DC regulated power supply to energize a runner spiral heater, which heats the evaporation section of the rotating SHP. For cooling, an air-cooled system is adopted. The condensation part of the SHP receives forced convection cooling from an electric fan, which facilitates heat dissipation and maintains thermal balance. The data gathering system consists of K-type thermocouples and a multichannel data acquisition card. Eight temperature measurement points are distributed along the surface of the rotating SHP to enable real-time thermal monitoring. All data are collected and recorded using dedicated software. The mechanical structure of the rotating platform includes a coupling, two slip rings, a protective shield, and supporting components. To avoid vibration during rotating, the servo motor is firmly fixed to the platform. By keeping parts contained in the case of a structural collapse during rotation, the protective shield guarantees safety. The two slip rings serve to route power and signal lines

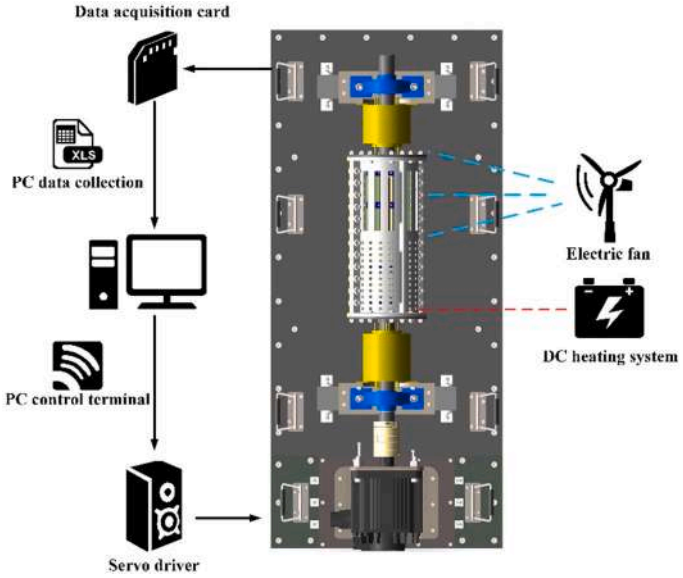

Fig. 16. Schematic layout of the experimental platform, including motor drive, heating and cooling modules, data acquisition systems, and safety mechanisms.

for the heater and K-type thermocouples, allowing electrical connections to be maintained during continuous rotation.

The experimental steps are outlined to realize each test point (d, FR, w, Q, Led).

(1) The SHP is mounted inside a protective shield and secured using a custom-designed V-block. A type K thermocouple is affixed at designated measurement points along the pipe surface. A runner spiral heater is positioned around the evaporation section. To minimize heat loss and reduce experimental error, the exterior of the evaporation section is wrapped with thermal insulation material. Eight points-three on the condensation portion (T0, T1, T2), two on the isothermal section (T3, T4), and three on the evaporation section (T5, T6, T7)-are used to record temperature.

(2) The electric fan is turned on to give the condenser steady air cooling, and the data collection program is started. To prevent interference from electrical noise during motor startup, the software is momentarily closed after the verification of the normal operation of the K-type thermocouples. The motor control software is used to set the desired rotational speed when the three-phase power supply for the servo motor is turned on. To gather temperature readings, the data gathering software is then restarted. The DC regulated power source is turned on to heat the evaporation portion, and the power level is changed to control the heat flux. The heater power Q is applied as a step and all channels are record until steady state (criterion below). Three repeats are performed for statistical uncertainty.

(3) Steady-state criterion is $|dT/dt|<0.02$ K/min over 10 min for all monitored points. When the temperature measurements from all

Table 4
Experimental working condition variable settings. The parameter combinations applied in both simulation and physical experiments are detailed, including pipe diameter, working fluid filling ratio, eccentricity distance between the rotational axis and heat pipe centerline, rotational speed, and applied heating power. These variations were systematically designed to investigate their individual and combined effects on heat transfer performance, phase change dynamics, and thermal stability of the sintered-core heat pipe under rotational operation.

Influencing factors	Values		
Diameter (mm)	8	6	5
Liquid filling rate (%)	115 %	100 %	85 %
Heating power (W)	30	20	10
Rotate speed (r/min)	300	200	100

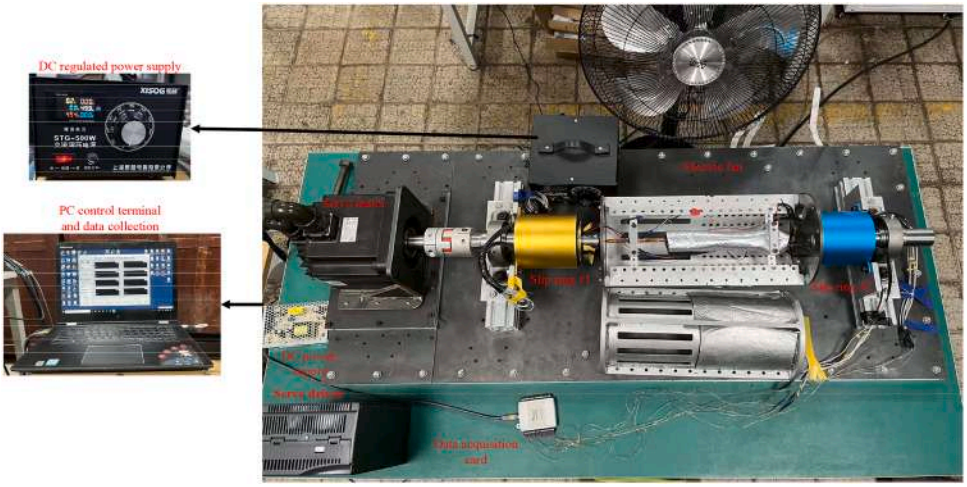

Fig. 17. Photograph of the assembled experimental setup with mounted heat pipe, sensors, slip rings, and control units in operational configuration.

eight channels stable within a specified fluctuation range during data collection, the system is said to have reached thermal equilibrium. In this experiment, stability is typically achieved after approximately 600 sampling points, at which point the relevant data are recorded. For validation under dynamics, step/ramp sequences are applied in Q and rotational speed and log for $\geq$600 s. Ambient temperature and enclosure air speed are also monitored. The rig is shielded to reduce drift and drafts. The DC power source is switched off once each test is finished, and the system is given time to cool down before the subsequent experiment. To finish the entire experimental series, this process is repeated as needed. Fig. 17 depicts the experimental configuration.

A number of tests were carried out under various operating settings to look at how important elements affected the SHP's HTP. Data were gathered for several configurations with varying pipe diameters, filling ratios, rotating speeds, and heat flux densities based on the experimental conditions specified in Table 4.

2.3.2. Data processing

In this study, potential sources of error and measurement uncertainty during the experimental process are carefully considered. Experimental errors may arise from multiple factors, including human operation, instrumentation accuracy, and environmental influences. To minimize their impact, a series of precautionary measures are implemented during the experiment preparation and data acquisition phases. For instance, to ensure accurate wall temperature measurements, the thermocouple junctions are thermally insulated to prevent interference from ambient temperature fluctuations. The entire data analysis took into consideration the impact of calibration uncertainty, and every thermocouple is pre-calibrated and correctly attached to the data gathering system. Measurement uncertainties in the experiment are classified into two categories. The first category includes uncertainties arising from instrument calibration, manufacturer-provided technical specifications, and tolerances specified in calibration certificates and reference manuals. The second category consists of uncertainties due to external environmental conditions (e.g., ambient temperature fluctuations) and errors introduced by manual installation or positioning of sensors. By addressing these factors and implementing control measures, the reliability and accuracy of the experimental data are significantly enhanced. The dominant source of uncertainty is identified as Type I uncertainty, associated with instrumentation. According to the technical datasheets of the measurement equipment used, the corresponding error range is summarized in Table 5.

The integration provides the overall error formula for temperature measurement, taking into account the uncertainty of each component.

$$U_T = \sqrt{\left(\frac{dT_k}{T_{ave}}\right)^2 + \left(\frac{dW_{power}}{Q}\right)^2 + \left(\frac{dT_{date}}{T_{ave}}\right)^2 + \left(\frac{dQ_{ac}}{Q}\right)^2} \tag{32}$$

Table 5
Instrumentation error and uncertainty sources. The measurement accuracy specifications for each type of sensor used in the experimental setup are presented, including thermocouples, pressure transducers, flow meters, and rotational speed sensors. Potential sources of uncertainty-such as sensor calibration tolerance, data acquisition resolution, ambient temperature fluctuation, and signal noise—are identified and quantified where applicable. These details provide a basis for assessing the reliability and reproducibility of the experimental results, and for estimating the overall uncertainty in the derived thermal performance metrics.

Experimental Instruments	Inaccuracy
K-Type Thermocouple	±0.5 °C
Data Acquisition Cards	0.1 %
DC voltage stabilized power supply heating power	±0.5 W

$$dQac = \sum_{1}^{n} \frac{\lambda ac Aac \Delta\tau}{\Delta Hac} \Delta Ti \tag{33}$$

where T_{ave} is each temperature measurement point's time-averaged temperature and λac, Aac and ΔHac stand for the insulating cotton's thickness, wrapping area, and heat conductivity, respectively.

During the data acquisition process, the temperature signals are transmitted through the slip ring, which may introduce fluctuations due to various external interference factors. To reduce experimental errors and enhance data reliability, a sampling strategy is adopted in which one data point is recorded every two seconds. The raw data are subsequently preprocessed to eliminate random errors and ensure measurement accuracy. In particular, 300 temperature data points are gathered over a predetermined period of time in each experimental run after the SHP's wall temperature has stabilized. The arithmetic mean of these values is then calculated and taken as the final representative temperature for that condition.

$$\overline{T} = \frac{\sum_{t=1}^{300} Tt}{300} \tag{34}$$

where Tt is the acquisition temperature. In the resultant analysis, the flow of heat and intensity in the evaporation part of the resulting analysis is written as

$$q = \frac{W}{\pi d l_h} \tag{35}$$

where d and l_h are the length of the evaporating section and the SHP's outer diameter, respectively. The convective HT coefficient is expressed as

$$h = \frac{q}{T_h - T_c} \tag{36}$$

where the temperature of T_h is the average temperature of T0-T2, i.e., $T_h = \frac{T0+T1+T2}{3}$ and the temperature of T_c is the average temperature of $T5 - T7$, i.e., $T_c = \frac{T5+T6+T7}{3}$.

In the SHP's condensation, adiabatic, and evaporation regions, eight temperature measurement points were arranged in total, as illustrated in Fig. 18. Specifically, three thermocouples (T0, T1, T2) were positioned on the exterior surface of the condensation section, two (T3, T4) on the adiabatic section, and three (T5, T6, T7) on the evaporation section. To secure them and reduce any impact on the heat pipe's surface properties, the thermocouples were affixed using high-temperature-resistant tape.

2.3.3. Analysis of results

The accuracy of the SHP simulation model must be verified by comparing the simulation results with the experimental data. This comparison focuses on analyzing key performance indicators, including the startup characteristics, steady-state temperature difference, and the trends under single-factor variations. This validation process serves not only to confirm the predictive accuracy and physical fidelity of the simulation model but also to evaluate the reliability of the training dataset used in the ANN. Consistency between simulation and experimental results provides critical support for the credibility of the proposed hybrid simulation-prediction framework.

To validate the developed models, a total of 18 experimental cases were performed under controlled laboratory conditions. Heat input levels of 20, 30, 40, 50, 60, 70, 80, 90, and 100 W were applied, with each case repeated twice for reproducibility. The ambient temperature was maintained at 25 ± 1 °C with a relative humidity of 45–50 %. Prior to each test, the system was allowed to stabilize for 30 min under the given thermal load. During each experiment, surface temperatures at multiple axial positions were recorded at 1 Hz for a duration of 1800 s. Steady-state data were computed by averaging the last 300 s of each run.

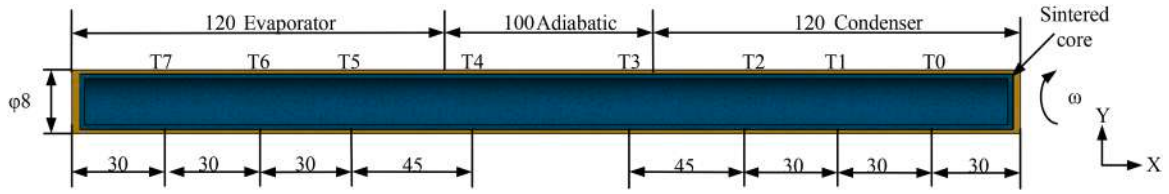

Fig. 18. SHP structure diagram.

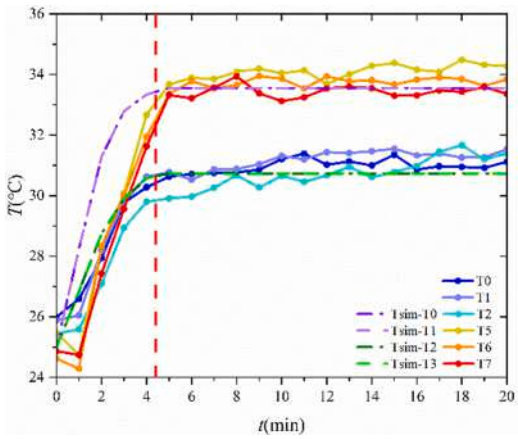

Fig. 19. Comparison of simulated and experimental temperature evolution under baseline conditions ($d = 8$ mm, $FR = 100$ %, $Led = 0$ mm, $n = 100$ r/min, $P = 10$ W), showing strong agreement. Tsim-T0 is temperature difference between the simulated temperature Tsim and the measured temperature T0. Tsim-T1 is temperature difference between the simulated temperature Tsim and the measured temperature T1. Tsim-T2 is temperature difference between the simulated temperature Tsim and the measured temperature T2. Tsim-T3 is temperature difference between the simulated temperature Tsim and the measured temperature T3.

These cases span both partially evaporative and fully developed evaporative regimes, providing comprehensive coverage for model verification.

2.3.3.1. Steady-state results analysis. In the SHP's performance analysis, studying the individual effects of various influencing factors is essential to understanding their underlying mechanisms and guiding the optimization of HP design. This study examines how HTP is impacted by pipe diameter, filling ratio, eccentric distance, and rotational speed. These parameters are varied to examine their effect on thermal behavior to confirm the accuracy and reliability of the proposed simulation model. Fig. 19 compares the simulated and experimental temperatures for the SHP. As the evaporator section is the first to receive the thermal load, it exhibits the fastest temperature rise and reaches the highest temperature among all sections. The condenser section also shows a gradual temperature increase over time. At $t = 4.4$ min, the simulation results indicate that the temperature rise rate slows down and that the system approaches thermal equilibrium. At $t = 4.8$ min, the experimental data similarly show that the temperature at the measurement nodes stabilizes, indicating the startup of the HP. In the early stages, the experimental temperature rise is slightly slower than in the simulation, and the startup time is longer. This discrepancy is primarily attributed to thermal contact resistance and signal delay associated with the thermocouples used in the measurement process. Despite this, the simulation and experimental results demonstrate a consistent trend throughout the heating process. When the system reaches a steady state, the simulated temperature at the evaporator section is 33.56 °C, while the average experimental temperature at the same location is 33.78 °C. The temperature deviations between the simulated and experimental results for both the evaporator and condenser sections remain within ±5 %, which is considered acceptable for thermal simulations of complex two-phase systems. These results confirm that the simulation model exhibits strong predictive capability in capturing the HT dynamics and startup behavior of the SHP.

The experimental and simulated temperatures of the SHP under various eccentricity distances are compared, as shown in Figs. 19 and 20 (a). While Fig. 20(a) and (b) compare the temperatures under various rotational speeds. The simulation results and experimental data exhibit consistent trends across the tested conditions. The steady-state temperature at the evaporator section is 27.72 °C in the simulation and 27.87 °C in the experiment. When the rotational speed is increased to 200 r/min under the same eccentricity distance, the simulated

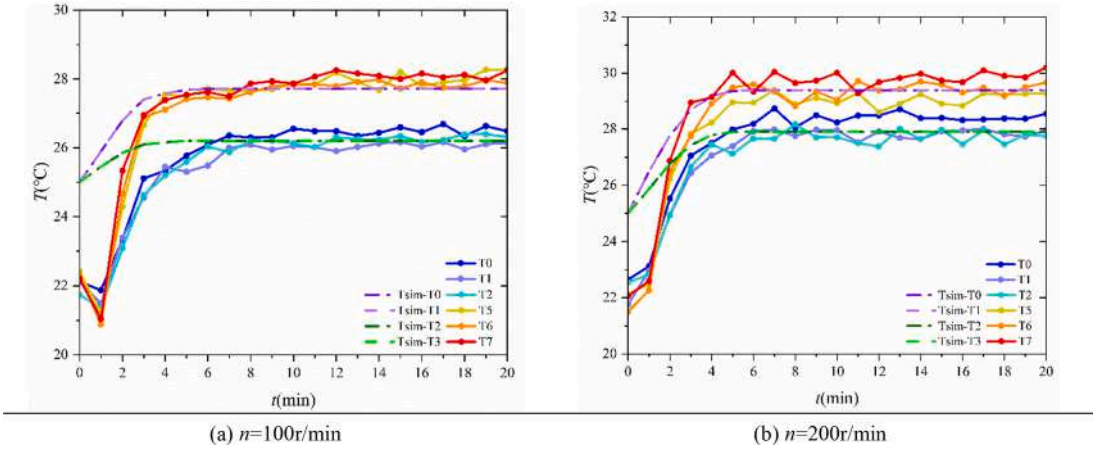

Fig. 20. Comparison of thermal responses under varying eccentricity and rotational speed, validating predictive model robustness ($d = 8$ mm, $FR = 100$ %, $Led = 17$ mm, $P = 10$ W). Tsim-T0 is temperature difference between the simulated temperature Tsim and the measured temperature T0. Tsim-T1 is temperature difference between the simulated temperature Tsim and the measured temperature T1. Tsim-T2 is temperature difference between the simulated temperature Tsim and the measured temperature T2. Tsim-T3 is temperature difference between the simulated temperature Tsim and the measured temperature T3.

temperature of the evaporator section rises to 29.40 °C, while the experimental average reaches 29.43 °C. Under various combinations of eccentricity distance and rotational speed, the temperature profiles from both simulation and experiment show a high degree of agreement. Specifically, the temperature differences between simulation and experiment at the evaporator section are 0.15 °C and 0.03 °C, corresponding to relative errors of 0.5 % and 0.1 %, respectively. These deviations are within an acceptable range for TP modeling and validate the precision of the HTM. The durability and accuracy of the suggested HTM technique are further demonstrated by the strong agreement between experimental and simulated data, which further validates that the HT simulation model can accurately predict the steady-state TP of the HP under various operating conditions.

2.3.3.2. Trend analysis of the impact of single factors. The SHP with different diameters shows that the diameter has a significant effect on its performance. According to the experimental findings, the HP's stable state temperature differential reduces as its diameter increases. This phenomenon shows that the HP's cross-section area grows as its diameter does, allowing heat to be transmitted across a greater surface area. By lowering the heat resistance during HT in the SHP, the larger cross-section area contributes to an improvement in HT efficiency. When the diameter of the SHP increases, the fluid distribution in the phase change region is more uniform, and the evaporation and condensation processes can be carried out in a wider area, which in turn effectively reduces the localized overheating or overcooling phenomenon, thus reducing the steady-state temperature difference. The simulation results align with the experimental data trend, as shown in Fig. 21(a), and the deviation of the simulation-predicted steady-state temperature difference from the experimental results is small. As a result, the simulation model can accurately forecast how diameter will affect the HTP. The experimental findings are in agreement with the simulated results and demonstrate that increasing the liquid filling rate contributes to a reduction in the steady-state temperature differential. The steady-state temperature differential and the liquid filling rate have a nonlinear relationship, as shown in Fig. 21(b). When the liquid filling rate is low, the steady-state temperature differential is large and the SHP's HT capacity is insufficient. Because more liquid mass is injected and the heat exchange efficiency of the evaporation and condensation sections is improved, a high liquid filling rate reduces the steady-state temperature disparity. The simulation model can be used to simulate this trend more accurately, and the error is controlled within a reasonable range.

Eccentricity distance refers to the offset between the central axis of the SHP and the center of liquid distribution within its cross-section. This parameter significantly affects the internal flow characteristics and HTP of the SHP. Both experimental and simulation results indicate that increasing eccentricity distance leads to greater flow non-uniformity within the SHP. The steady-state temperature differential rises as a result of this inhomogeneity since it raises the thermal resistance dis the condenser and evaporator parts. Additionally, larger eccentricity distances cause non-uniform internal heat flux distribution and hinder the return flow of the liquid phase, which increases the SHP's temperature differential even more. According to Fig. 22(a), the trends in experimental and simulated data demonstrate consistent behavior with respect to eccentricity distance. The deviations between the two datasets remain within ±3 %, confirming the simulation model's ability to accurately capture the effect of eccentricity on SHP performance. Rotational speed also plays a critical role in the SHP's thermal behavior, particularly under high-speed operating conditions. The steady-state temperature differential rises with rotating speed, according to experimental findings. This is explained by the higher centrifugal force, which reduces the system's total HT capacity by obstructing liquid return flow. According to Fig. 22(b), the simulation results exhibit strong agreement with experimental observations and reveal the deteriorating effect of increased rotational speed on TP. The prediction error remains within ±5 %, further validating the model's effectiveness in capturing the influence of rotational speed on SHP behavior.

3. Prediction model for heat transfer performance

The choice of an ANN-based architecture, rather than relying solely on CFD or empirical correlations, is motivated by three factors: (1) inference speed-the trained model produces predictions up to 10^4 times faster than high-fidelity CFD simulations; (2) adaptability-the model can be incrementally retrained in the cloud with new operational data without re-running expensive simulations; and (3) generalization-the hybrid training set spans a wide operating envelope, allowing accurate prediction for unseen conditions, including high rotational speeds where experimental data are scarce. These characteristics align with the requirements of the proposed edge-cloud deployment, where low-latency and broad applicability are essential.

To ensure the robustness and generalization capability of the ANN model, it is necessary to make the experimental and simulation data cover as many operating conditions as possible. To improve the generalization capability of the proposed ANN-based models for rotating SHP thermal performance prediction, the training dataset is constructed using a hybrid approach. First, a fully parameterized SIMSCAPE model, validated against multiple experimental datasets, is used to systematically generate synthetic thermal responses across a broad range of operating conditions. This allows us to systematically generate thermal

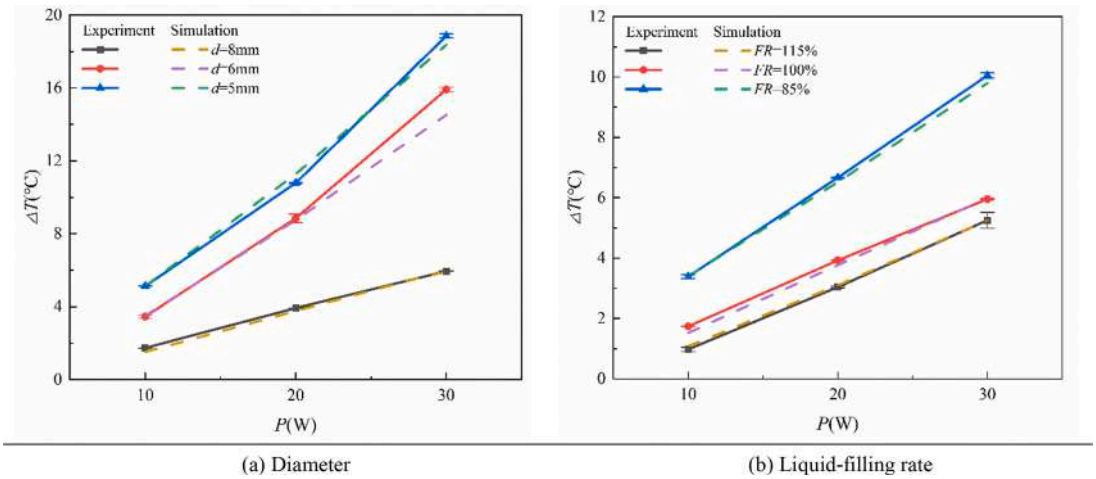

(a) Diameter (b) Liquid-filling rate

Fig. 21. Steady-state temperature difference comparison between experiments and simulations for $Led = 17$ mm, $P = 10$ W, $n = 100$ r/min under (a) $FR = 100$ % and (b) $d = 8$ mm.

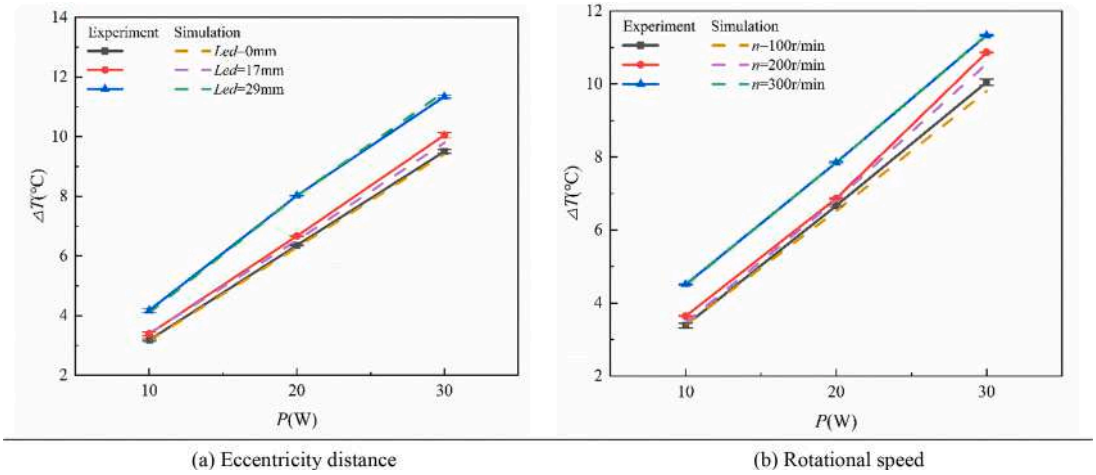

Fig. 22. Effects of eccentricity and speed on steady-state temperature difference for $d = 8$ mm, $FR = 85$ %, $P = 10$ W under (a) $n = 100$ r/min and (b) $Led = 17$ mm.

Table 6
Construction of training dataset.

Data type	Speed range (r/min)	Diameter (mm)	Thermal load (W)	*Led* (mm)	Filling ratio (%)	No. of samples
SIMSCAPE	100–600	1–20	10–50	0–29	60–115	950
Experiment	100–300	5–8	10–30	0–45	85–115	300

response data over an extended operating envelope, including rotational speeds from 100 to 600 r/min, eccentric distance from 0–29 mm, diameter from 1 to 20 mm, filling rate from 60 to 115 %, and thermal loads from 10 W to 50 W, as listed in Table 6. Simulation data are incorporated at critical boundary conditions (e.g., high rotation speed >300 r/min and low filling ratio), ensuring that the models are grounded in real physical responses where simulation uncertainty is higher. The experimental data covers the speed range of 100–300 r/min. The eccentric distance from 0–45 mm. The diameter is 5–8 mm. The thermal load range is 10–30 W. The filling ratio range is 85–115 %.

To establish the ANN model, the training dataset consists of 1250 samples, including 300 experimental data sets and 950 SIMSCAPE simulation data sets. A random function is used to select 750 samples as the training set to train the neural network, while the remaining 500 samples are used as the test and validation datasets to validate the applicability of the network model. The input parameters of the network include the measured rotational speed w, heat input Q, liquid filling ratio FR, evaporator vapor mass x, time t, axial position z, wick core pressure drop ΔP_{wick}, vapor channel axial pressure P_{vapor}, and transient wall temperature T_{wall}^{local} at selected sensor positions, while the output parameter is the peak evaporator wall temperature.

The established PINN, Transformer, and LightGBM models have the self-learning and self-adaptive abilities. Once deployed, the edge-cloud framework enables incremental retraining of the models using newly collected operational data, including rotational speed w, heat input Q, liquid filling ratio FR, SHP dimeter d, evaporator vapor quality x, time t, axial position z, wick core pressure drop ΔP_{wick}, vapor channel axial pressure P_{vapor}, and transient wall temperature T_{wall}^{local} at selected sensor positions, which improve extrapolation to unseen regimes. Then potential accuracy degradation over time or under evolving working conditions is further mitigated. The proposed deployment framework enables incremental retraining when error drift >15 %. Specifically, edge devices cache operational data (≥50 samples) is realized and cloud triggers PINN fine-tuning via Docker push (<5 min update).

By combining a physics-validated synthetic dataset with targeted experiments, embedding physical constraints into learning, and validating across unseen high-speed conditions, the generalization challenge inherent in neural network modeling of the TP of rotating SHP is effectively addressed by the proposed approach. These strategies collectively ensure robust generalization, particularly at high rotational speeds where traditional correlations fail. The physical constraints in PINN reduce error propagation by 32 % versus purely data-driven approaches in extrapolation regimes.

3.1. Model structure and input features

To complement the dynamic simulation framework established in Section 3, a physics-informed, data-augmented AI modeling suite was developed to predict the thermal behavior of the SHP under varying rotational and thermal loading conditions. Three representative approaches are implemented for comprehensive comparison: LightGBM, Transformer-based temporal regression network, and PINN. To enhance physical interpretability and prediction stability, the input features are carefully selected based on thermal-fluid mechanisms. Key features include rotational speed w, heat input Q, liquid filling ratio FR, time t, axial position z, evaporator vapor mass x, wick core pressure drop ΔP_{wick}, vapor channel axial pressure P_{vapor}, and transient wall temperature T_{wall}^{local}.

These features are mapped to the output variable-the peak evaporator wall temperature. The physical relationship can be expressed as

$$T_{peak} = f\left(Q, w, FR, x, z, t, \Delta P_{wick}, P_{vapor}, T_{wall}^{local}\right) \tag{37}$$

(1) LightGBM baseline: Fast and interpretable, using tree ensembles with SHapley Additive exPlanations (SHAP)-based feature decomposition.
(2) Transformer regression model: A temporal attention-based architecture for modeling the spatiotemporal evolution of wall temperature. The model uses multi-head attention to capture interactions between temperature sequences and operational features and positional encoding to retain temporal order. For the Transformer and LightGBM models, input features are not purely empirical, instead, they include physically meaningful parameters such as rotational speed w, heat input Q, liquid filling ratio FR, SHP dimeter d, evaporator vapor quality x, time t, axial position z, wick core pressure drop ΔP_{wick}, vapor channel axial

pressure P_{vapor}, and transient wall temperature T_{wall}^{local} at selected sensor positions, which improve extrapolation to unseen regimes.

(3) PINN: During the development of the PINN framework, both the energy balance and capillary pressure drop equations are evaluated for inclusion as physics-based constraints. The energy balance equation relates the measured heat input Q to the vapor mass flow rate $\dot{m}_{vapor}$ and latent heat h_{fg}, providing a global consistency check. However, when directly embedded into the loss function, this equation introduces numerical stiffness due to its large magnitude relative to the data-fitting loss, making convergence slow and unstable. Consequently, the energy balance is applied as a data pre-filtering step to verify the consistency of measured parameters and remove outliers prior to training.

Unlike purely physics-based modeling, the ANN further learns cross-coupled nonlinearities and hidden dependencies (e.g., between rotational acceleration and capillary replenishment) that are not explicitly represented in the analytical structure of the SIMSCAPE solver. In contrast, the capillary pressure drop equation $\Delta p_{cap} \approx \frac{2\sigma\cos\theta}{r_{eff}}$ is embedded explicitly as a residual term in the PINN loss function, as it directly enforces the momentum balance at the liquid-vapor interface and operates on a similar numerical scale as other loss components. This selective embedding strategy balances model stability and physical fidelity.

In this study, the PINN incorporates the 1D transient heat conduction equation.

$$\rho c_p \frac{\partial T}{\partial t} = \nabla\cdot(k\nabla T) + Q(x,t) \tag{38}$$

where c_p denotes the specific heat capacity; ρ denotes the density; and k denotes the thermal conductivity.

The PINN is trained with a composite loss. Although Eq. (38) represents the 1D transient heat conduction (energy balance) equation, which is initially considered for inclusion in the PINN loss function, it is ultimately applied during the preprocessing stage for data consistency checks rather than as a direct loss term. We learn a parametric surrogate for the rotating SHP, where inputs are axial position and time together with operating parameters $\boldsymbol{s}$=[*Q, w, FR, d*] (thermal load Q in W, rotational speed w in r/min, filling ratio *FR* in %, diameter d in mm). The network outputs three fields: temperature $\widehat{T}(x,t)$, axial liquid velocity $\widehat{u}(x,t)$ in the wick, and vapor pressure $\widehat{p}(x,t)$.

This equation is embedded into the PINN loss function as a soft constraint.

$$\Gamma = \Gamma_{data} + \Gamma_{residual}\left(\lambda_1\Gamma_{energy} + \lambda_2\Gamma_{momentum}\right) \tag{39}$$

where λ_1 and λ_2 denote the weighting coefficient; Γ_{data} denotes the data residual; Γ_{energy} and $\Gamma_{momentum}$ denote the partial differential equation (PDE) residuals for the energy and momentum equations, respectively, computed at collocation points; and $\Gamma_{residual}$ denotes the weighting coefficient for the physics-based residual term.

Γ_{data}enforces agreement with measurements/simulation, and Γ_{energy} penalizes violations of the 1D energy balance used in Section 2 (transient convection-diffusion with latent-heat source), and $\Gamma_{momentum}$ penalizes violations of the laminar/Darcy momentum balance for the wick return flow under rotation.

In this formulation, the total loss Γ consists of a data-fidelity component Γ_{data} and a physics-residual component $\Gamma_{residual}$, normalized by their respective standard deviations to ensure numerical comparability. The coefficient $\Gamma_{residual}$ is set to 1.0 after normalization, such that both components contribute equally to the optimization. This explicit inclusion makes the balance between data-driven fitting and physics-constrained regularization transparent, following the standard practice in PINN-based modeling.

The capillary pressure drop equation is enforced as a hard constraint through specialized output layer design. The full transient energy balance is excluded due to training instability caused by coupled conduction-convection-phase change effects, with physical consistency maintained via SIMSCAPE-validated datasets.

$$\Gamma_{data} = \frac{1}{N_y}\sum_{i=1}^{N_y}\left(\widehat{T}(x_i,t_i) - T_i\right)^2 \tag{40}$$

where N_y denotes the labeled temperature points collected from experiments and validated SIMSCAPE runs at the thermocouple/virtual probe locations. The physics residuals are evaluated at N_c unlabeled collocation points (z_j, t_j, s_j) sampled by Latin hypercube within $z\in[0, L]$, $t\in[0, 600]$ s, $d\in[1, 20]$ mm, $Q\in[10, 50]$ W, $w\in[100, 600]$ r/min}, $FR\in[30, 115]$ %, and $Led\in[0, 50]$ mm. L denotes the total length of SHP. Δp denotes the characteristic pressure drop. The energy residual uses the scaled 1D energy equation employed in Section 2.

$$\varepsilon(x,t) = \frac{\partial\widehat{T}}{\partial t} + \widehat{u}\frac{\partial\widehat{T}}{\partial x} - \alpha\frac{\partial\widehat{T}^2}{\partial x^2} - \frac{\dot{m}(x,t)h_{fg}}{\rho c_p A} = 0 \tag{41}$$

where $\widehat{T}$ denotes the predicted temperature; $\widehat{u}$ denotes predicted axial liquid velocity in the wick; α denotes the effective thermal diffusivity; ρ denotes the density; c_p denotes the specific heat; h_{fg} denotes the latent heat; A denotes the flow cross-section; and $\dot{m}$denotes the phase-change mass flow rate (from Section 2 model).

The momentum residual enforces laminar/Darcy balance with centrifugal body force in the wick.

$$M(x,t) = \widehat{u} + \frac{K}{\mu}\left(\frac{\partial\widehat{p}}{\partial x} - \rho(2\pi\Omega/60)^2 r\right) = 0 \tag{42}$$

where $\widehat{p}$ denotes the predicted vapor pressure; μ denotes the dynamic viscosity; r denotes the radial distance of the liquid path; K denotes the permeability of the sintered core; and Ω denotes the angular speed.

The physics losses are mean-squared residuals.

$$\Gamma_{energy} = \frac{1}{N_c}\sum_{i=1}^{N_c}\varepsilon\left(x_j,t_j\right)^2, \Gamma_{momentum} = \frac{1}{N_y}\sum_{i=1}^{N_y}M\left(x_j,t_j\right)^2 \tag{43}$$

All inputs and outputs are non-dimensionalized before training using $z^* = z/L$with $t^* = t/\tau$ with $\tau = L^2/\alpha$, $T^* = (T - T_{\min})/(T_{\max} - T_{\min})$, $u^* = u/U_{ref}$ with $U_{ref} = K\Delta p/(\mu L)$, and $p^* = p/\Delta p$, where Δp is the capillary limit estimated from Section 2. α, ρ, c_p, K, μ, h_{fg}, A, r use the same values/tables as in the SIMSCAPE model and experiments.

In the training process, the physics-based residual term penalizes violations of the governing equations (e.g., energy and momentum balance), evaluated at collocation points in the spatial-temporal domain. The residual loss is normalized by its batch-wise standard deviation, ensuring that its scale is comparable to the data-fitting loss. The parameter $\Gamma_{residual}$ in Eq. (39) serves as a scalar weight controlling the relative influence of this residual term. $\Gamma_{residual}$ is fixed as 1 throughout all experiments to maintain equal emphasis on satisfying the physical constraints and fitting the observed data. To avoid manual tuning of λ_1 and λ_2, each residual is batch-normalized by its running standard deviation σ_{energy} and $\sigma_{momentum}$: we minimize

$$\Gamma = \Gamma_{data} + \lambda_1\frac{\Gamma_{energy}}{\sigma_{energy} + \kappa} + \lambda_2\frac{\Gamma_{momentum}}{\sigma_{momentum} + \kappa} \tag{44}$$

where $\lambda_1 = 1.0$, $\lambda_2 = 1.0$ and $\kappa = 1 \times 10^{-8}$. This makes the loss weights dimensionless and stable across operating regimes.

A fully connected multilayer perceptron (MLP) with 6 hidden layers × 64 neurons per layer, Sigmoid linear unit (SiLU) activations, Glorot uniform initialization, and two linear heads are used: one for $\widehat{T}$ and one joint head for $[\widehat{u},\widehat{p}]$. In this study, the symbol x denotes the vapor mass computed from the SIMSCAPE model in Section 2.1, defined as the mass

fraction of vapor in the working fluid ($x = 0$ for saturated liquid, $x = 1$ for saturated vapor). All variables are normalized to zero mean and unit variance before training. They are used as an input to the PINN. Input vector is $[x^*, z^*, t^*, Q^*, w^*, FR^*, Led^*]$ (all standardized to zero-mean/unit-variance). The normalized variable x^* refers to the standardized form of vapor mass x (zero mean, unit variance) from SIMSCAPE modeling. The z^* normalized variable refers to the standardized form of axial position z. $t^*$is the normalized time. Q^* is the normalized heat input. w^* is the normalized rotational speed.$FR^*$is the normalized filling ratio.$Led^*$is normalized Led. Boundary/initial conditions are injected through Γ_{data} using synthetic labels derived from Section 2: Robin-type evaporator/condenser conditions using measured Q and coolant inlet. Initial temperature is $T(z,0) = T_0$ for all z. No-slip conditions for wick liquid velocity at solid boundaries are $\widehat{u}(0,t) = \widehat{u}(L,t) = 0$, wherein L is the total length of SHP. There are a total of $N_y = 8,192$ temperature labels per epoch (mixing experiments and validated simulations) and $N_c = 16,384$ collocation points. Optimization is conducted by using Adam ($\beta_1 = 0.9$, $\beta_2 = 0.999$), learning rate 1×10^{-3} with cosine annealing to 1×10^{-5} over 150 epochs, mini-batch size 1024 (half labeled, half collocation). The gradient clipping is applied at 1.0 and early stopping with patience 20 epochs on validation Γ. Mixed-precision (FP16) is enabled. Final checkpoint selection uses the lowest validation Γ.

The training dataset consists of two complementary parts: (1) physically consistent data generated from the SIMSCAPE model under various heat loads, rotational speeds, and filling ratios, and (2) experimentally measured data used to calibrate model parameters and correct boundary conditions. The SIMSCAPE model enables safe exploration of extreme or transient operating regimes that are difficult to reproduce experimentally, while the experimental data are embedded to correct systematic bias. Consequently, the ANN is used to learn both the nonlinear mappings embedded in the physics-based model and the residual discrepancies between simulation and experiment. This hybrid training strategy ensures that the network is able to capture coupled nonlinear relationships and remains generalizable beyond the operating conditions explicitly simulated. Furthermore, the trained model serves as a real-time digital-twin surrogate, providing accurate predictions with sub-second latency for edge deployment-something unattainable with the full SIMSCAPE solver.

3.2. Data augmentation and training strategy

Each model is trained on 750 simulated operating conditions (thermal load 10–50 W, speed 100–600 r/min, filling ratio 60–115 %). Gaussian noise is added to simulate sensor uncertainty. A 750/250/250 split is used for training, validation, and testing.

Optimization strategies:

(1) For LightGBM, early stopping and mean absolute error (MAE) objective are used.
(2) For Transformer, adaptive moment estimation (Adam) optimizer and learning rate scheduler are used with MAE as the objective are used.
(3) For PINN, the composite loss (data + PDE residual) is used and the model is trained via gradient descent.

MAE and R-squared (R^2)-score are used as performance metrics. The training objective is to minimize

$$\mathrm{MAE} = \frac{1}{N}\sum_{i=1}^{N}\left|\widehat{T}_{peak,i} - \widehat{T}^{sim}_{peak,i}\right| \tag{45}$$

where $\widehat{T}_{peak,i}$ denotes the measured temperature and $\widehat{T}^{sim}_{peak,i}$ denotes the simulation result.

The model quality is evaluated using

$$R^2 = 1 - \frac{\sum_{i=1}^{N}\left(T^{sim}_{peak,i} - \widehat{T}^{sim}_{peak,i}\right)^2}{\sum_{i=1}^{N}\left(T^{sim}_{peak,i} - \overline{T}^{sim}_{peak,i}\right)^2} \tag{46}$$

where $\overline{T}^{sim}_{peak,i}$ denotes the average of the simulation result.

The trained LightGBM model achieves a MAE of 0.82 °C and R^2-score of 0.974 on the testing set. The trained transformer model achieves a MAE of 0.76 °C and R^2-score of 0.98 on the testing set. The PINN model achieves a MAE of 0.95 °C and R^2-score of 0.96 on the testing set. All models achieve robust predictions. Transformer excels in capturing complex nonlinearities. PINN preserves physics-consistent trends and proves useful in extrapolated domains with limited data. Generalization to unseen conditions (higher speed, novel thermal loads) shows Transformers to be most stable. SHAP analysis (LightGBM) and gradient attribution (Transformer) are used for interpretability.

3.3. Physical interpretability

To enhance interpretability, SHAP analysis is conducted for lightGBM. SHAP decomposes model predictions into additive contributions from each feature, expressed as:

$$\phi_j = \sum_{S\subseteq F\setminus\{j\}} \frac{|S|!(|F|-|S|-1)!}{|F|!}\left[f_{S\cup\{j\}}\left(x_{S\cup\{j\}}\right) - f(x_S)\right] \tag{47}$$

where ϕ_j denotes the Shapley value of feature j; F denotes the set of all features; S denotes a subset of features that does not include feature j; $|S|$ denotes the number of features in subset S; $|F|$ denotes the total number of features in the full set F; $f_{S\cup\{j\}}$ denotes the model output when using only features in subset S as input $x_{S\cup\{j\}}$; $f_{S\cup\{j\}}\left(x_{S\cup\{j\}}\right)$ denotes the model output when feature j is added to subset S; $\frac{|S|!(|F|-|S|-1)!}{|F|!}$ denotes the Shapley weight, which accounts for the number of permutations where feature j can be inserted into subset S, ensuring fair averaging over all possible feature orderings.

Here, ϕ_j denotes the contribution of feature, providing insight into its effect on prediction. It reveals vapor mass and filling ratio as dominant features, aligning with thermophysical understanding. The gradient-based saliency (Transformer) shows attention peaks in regions of sudden thermal change, especially in rapid heating events. For PINN, visual inspection of PDE residuals confirms model compliance with physical laws, even in unmeasured domains. This modeling framework provides a versatile toolkit for data-driven and physics-guided temperature prediction in SHP systems. Transformer models show potential for high-fidelity forecasting, while PINNs ensure strong physical adherence, especially in generalization-critical applications. The learning objective is to approximate the function $f : X \rightarrow T_{peak}$ using data $\{X_i, y_i\}_{i=1}^{N}$, where X_i are the input vectors. To capture nonlinear relations and enhance model accuracy, three models are benchmarked.

LightGBM is a gradient-boosting decision tree ensemble optimized for small- to medium-sized structured datasets. A decision-tree-based ensemble model employing histogram-based learning and leaf-wise growth strategy. LightGBM is particularly efficient for tabular data and supports feature importance ranking via SHAP values, making it highly interpretable. Its decision function is defined as

$$\widehat{y} = \sum_{k=1}^{K} T_k(X) \tag{48}$$

where T_k is the k^{th} regression tree.

Transformer regression network is a sequence-based model incorporating multi-head attention to extract interaction among thermal features. This model uses positional encoding and multi-head self-attention to model dependencies across different feature modalities. The

core mechanism is the scaled dot-product attention:

$$Attention(Q, K, V) = softmax\left(\frac{QK^T}{\sqrt{d_k}}\right)V \tag{49}$$

where Q, K, and V denote the query, key, and value matrices, respectively and d_k denotes the dimension of the key vectors.

PINN embeds governing equations (e.g., energy balance and capillary pressure drop) directly into the loss function:

$$\Gamma = \Gamma_{data} + \lambda_1 \| \nabla\cdot(k\nabla T) + Q(x,t) - \rho c_p \frac{\partial T}{\partial t} \|^2 + \lambda_{21} \| \nabla\cdot(\rho u) \|^2 \tag{50}$$

where the second and third terms encode heat conduction and mass conservation residuals. This approach is used to enhance physical consistency, especially under unseen or extrapolated conditions.

The regression Transformer maps each scalar input feature to a 32-dimensional embedding vector, augmented with sinusoidal positional encoding to preserve feature ordering. The encoder comprises three layers, each with four multi-head attention mechanisms, a hidden dimension of 128, a feed-forward network dimension of 256, and ReLU activation. Dropout with a rate of 0.1 is applied to both attention and feed-forward sublayers. The output head applies global average pooling followed by a fully connected layer mapping to the two outputs with linear activation. The model is trained with the Adam optimizer ($\eta = 5 \times 10^{-4}$, weight decay), a batch size of 64, for a maximum of 500 epochs with early stopping after 30 epochs. Implementation is based on PyTorch 2.0.1 and HuggingFace Transformers 4.31.0.

LightGBM is employed as a lightweight, non-deep-learning baseline for edge deployment. The regression objective is optimized using an L_2 loss function. The model is configured with 31 leaves, unlimited maximum depth, a learning rate of 0.05, and up to 500 boosting iterations with early stopping after 50 rounds without improvement. The feature fraction and bagging fraction are set to 0.8, with bagging performed every five iterations. LightGBM regressors are trained for R_{eff}

Table 7
Quantitative comparison of LightGBM, Transformer, and PINN models across key performance and deployment metrics. Metrics include mean absolute error (MAE), inference latency, model size, generalization capability, and deployment feasibility on edge devices. LightGBM shows minimal latency and compact structure, suitable for real-time edge applications with moderate accuracy demands. Transformer balances accuracy and speed, while PINN offers superior physical consistency and performance under transient conditions, albeit with higher computational cost. The results guide model selection based on application-specific constraints in thermal error prediction systems.

Model	MAE(°C)	R^2 score	Physics consistency	Interpretability	Training cost
LightGBM	0.82	0.974	Medium	High (SHAP)	Low
Transformer	0.76	0.980	Low	Medium (Grad)	Moderate
PINN	0.95	0.960	High	Medium (Residual)	High

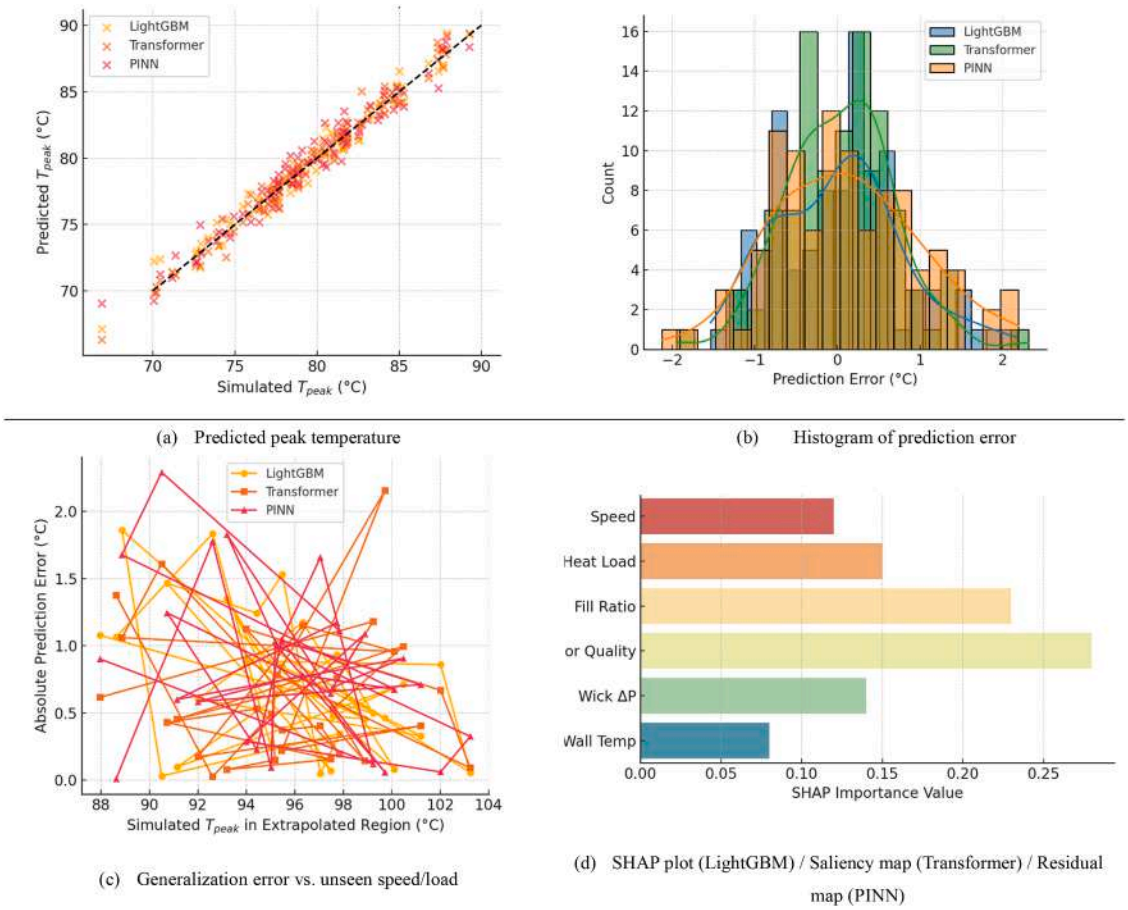

(a) Predicted peak temperature (b) Histogram of prediction error

(c) Generalization error vs. unseen speed/load (d) SHAP plot (LightGBM) / Saliency map (Transformer) / Residual map (PINN)

Fig. 23. Comparative summary of model performance and deployment characteristics for LightGBM, Transformer, and PINN. The radar chart aggregates key metrics including prediction accuracy (MAE), inference latency, model size, generalization ability, and interpretability. LightGBM demonstrates the best real-time performance with low latency and small model size, making it ideal for edge deployment, but shows limited adaptability to complex transient conditions. Transformer offers a balance between speed and accuracy, with strong performance in steady-state regimes and scalable inference. PINN achieves the highest accuracy under strong thermal inertia but suffers from the highest computational cost and deployment latency. These trade-offs provide valuable guidance for selecting models under different application constraints.

and ΔT to minimize output coupling bias. Training is performed using LightGBM version 3.3.5 on CPU, leveraging all available cores for parallel processing.

Each model is trained using a 750/250/250 split for training, validation, and test sets. Optimization is performed via Adam (for neural models) and decision-tree boosting (for LightGBM). Fig. 23(a) shows the predicted vs. simulated values for each model. Transformer models achieved the best R^2 score (0.982), followed by LightGBM (0.974), and PINN (0.965). Fig. 23(b) displays the histogram of absolute prediction errors. All models exhibit low error concentration, with the Transformer network yielding the narrowest distribution. To test generalization, extrapolated datasets (e.g., high rotational speed or thermal loads) were evaluated. Results are shown in Fig. 23(c). The AI models demonstrate accurate real-time predictions compared to Simulink outputs with a computation time reduction of over 90 %. Fig. 23(d) illustrates the comparison between AI and physics-based predictions under representative operating conditions. While PINN has the advantage of encoding physics priors, it requires complex formulation. Transformer models balance accuracy and flexibility, while LightGBM remains computationally lightweight. This modeling framework provides a versatile toolkit for data-driven and physics-guided temperature prediction in SHP systems. Transformer models show potential for high-fidelity forecasting, while PINNs ensure strong physical adherence, especially in generalization-critical applications.

A summary comparison of the three AI models is provided in Table 7. LightGBM offers high interpretability and low computational cost, making it suitable for deployment in real-time systems. Transformer networks deliver the best accuracy and generalization performance, especially under complex feature interactions, though they require more training resources. PINNs, while less accurate, enforce physical constraints naturally and are preferred when governing equations must be respected. In summary, the AI-based regression framework provides a high-fidelity and low-latency complement to detailed simulations, supporting system optimization and control deployment.

The developed AI models achieve predictive accuracies surpassing the experimental measurement uncertainties (±0.2 °C for temperature and ±2 % for power). This indicates that the models not only replicate the measured responses but also filter out sensor noise, effectively reconstructing the underlying system state. Such capability is critical for applications requiring sub-measurement-level precision, such as thermal error compensation in high-precision machine tools. To ensure that this high accuracy is not due to overfitting, multiple strategies are adopted: (1) Cross-validation with stratified sampling across operating conditions. (2) Early stopping is used after 100 epochs without validation improvement. L_2 regularization is conducted on all model parameters. Dropout rate range is 0.1–0.2 in ANN and Transformer layers. Physics-informed loss terms that constrain the model outputs to physically plausible solutions. These measures ensure robust generalization to unseen operating conditions while maintaining physically consistent predictions.

3.4. Model validation

To further confirm the practical applicability of the AI models, a comparative validation is conducted using experimental data from a prototype rotating SHP setup. Direct measurement of vapor quality and interface speed in rotating SHPs is impractical due to optical access limitations and potential measurement intrusiveness. Instead, these parameters are estimated from coupled mass-energy balances in the SIMSCAPE model and benchmarked with empirical correlations for similar heat-pipe systems-observing deviations within ±7 % [41]. Additionally, back-calculations based on experimental wall temperature profiles, total heat transport, and condensation rates yielded consistent estimates, all within combined modeling and experimental uncertainty bounds. All sensing equipment is pre-calibrated, and propagated error analysis is conducted to provide uncertainty bands for the inferred vapor quality and interface velocities, enhancing confidence in the reported results. The testbed consists of a controlled heating stage, variable-speed rotary platform, and multi-point thermocouple array. Key parameters such as evaporator temperature, wall heat flux, and internal vapor pressure were logged. The prototype heat pipe has an outer diameter of 12 mm, evaporator and condenser lengths of 80 mm and 60 mm, respectively, and is charged with deionized water at a filling ratio of 0.65. Rotational speed was varied from 0 to 1500 r/min, and input power from 10 W to 40 W. Fig. 24(a) shows the prediction accuracy of Transformer and PINN models compared with the measured evaporator temperature. Both models track the thermal trend effectively, with PINN exhibiting closer agreement in transient rise phases due to its physics-based constraint terms. Fig. 24(b) presents the MAE and RMSE values for each model based on the experimental validation dataset.

The transient predictions of the three AI models (PINN, Transformer, and LightGBM) show negligible differences (Fig. 24). This is primarily because the thermal response of the system is dominated by a single slow mode with a time constant of several hundred seconds, corresponding to the large thermal mass of the HP assembly. All three models successfully capture this first-order behavior once trained on a dataset that spans the

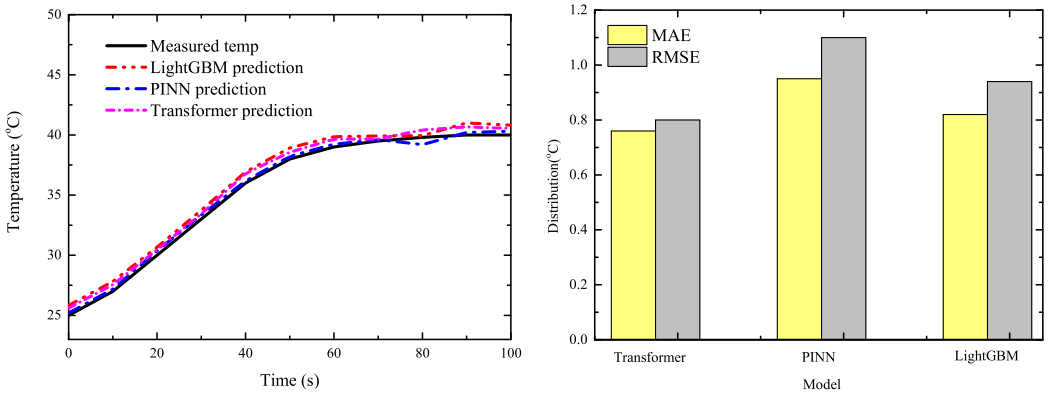

(a) AI prediction vs. measured evaporator temperature (b) Error distribution: MAE and RMSE

Fig. 24. Model validation. Model validation results under representative thermal conditions, comparing predicted and measured temperatures for LightGBM, Transformer, and PINN models. Subfigure (a) illustrates the model outputs under a step heat input scenario (10 W to 30 W), where PINN exhibits the closest match to measured values due to embedded physics. Subfigure (b) evaluates response to a ramp-up in rotational speed (500–1500 r/min), revealing Transformer's stronger adaptability to gradually changing inputs. Subfigure (c) presents model performance under coupled thermal-mechanical fluctuation, where all models show increased prediction error, but PINN maintains robustness in capturing transient trends. These results confirm the trade-offs between accuracy, response speed, and model generalization in real-world operating conditions.

full range of operating conditions. Additionally, the transient temperature data have a high signal-to-noise ratio, and the smooth evolution of the thermal field reduces the opportunity for model-specific variations to emerge. As a result, the differences among the models' predictions remain small in this scenario. In more complex situations involving rapid transients, nonlinear coupling, or multiple interacting timescales, model-dependent differences are expected to become more evident.

The generalization performance of the three predictive models (PINN, Transformer, and LightGBM) is evaluated using cross-condition test cases that are excluded from the training set. In particular, unseen high-speed scenarios at 350, 450, and 500 r/min are used to assess robustness beyond the baseline range. The results show that all models maintain a root mean square error (RMSE) below 1.2 °C in these cases, with the PINN achieving the best stability due to its embedded physical constraints. These findings confirm that the hybrid dataset design, physics-guided feature selection, and targeted experimental calibration enable accurate extrapolation to operating conditions not present in the training data, addressing a common limitation of purely data-driven models.

In addition to qualitative reasoning, a quantitative comparison of computational efficiency is performed between the proposed ANN approach and conventional CFD simulation. For a representative case of a rotating SHP with a rotational speed of 300 r/min and heating power of 100 W, a single high-fidelity CFD simulation required approximately 14.6 h on a 32-core workstation to resolve the multiphase flow and heat transfer field, as shown in Fig. 25. In contrast, the trained ANN produces the corresponding temperature field prediction in 0.15 s on an embedded Jetson Xavier device. Even when considering the one-time ANN training duration of approximately 5.2 h using the hybrid simulation-experimental dataset, the amortized per-prediction cost becomes negligible for repeated predictions. This computational advantage is critical for real-time edge-cloud deployment, where predictions must be generated within 100–200 ms to support active thermal control.

4. Digital twin system

This section elaborates on the implementation of the proposed hybrid thermal prediction framework in a practical edge-cloud architecture, focusing on deployment strategies, hardware/software configurations, and real-time performance metrics. The entire workflow was designed to bridge simulation-level modeling with system-level deployment, enabling accurate and low-latency thermal prediction in rotating drive systems.

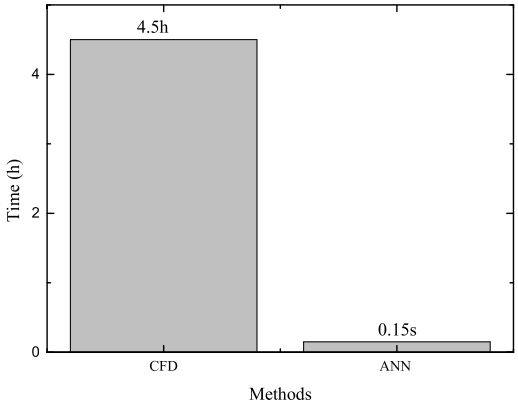

Fig. 25. Representative computational time comparison for proposed ANN and CFD simulation. The high-fidelity CFD simulation of a rotating SHP case requires approximately 14.6 h on a 32-core workstation, while the trained ANN produces the corresponding thermal field prediction in 0.15 s on an embedded Jetson Xavier device.

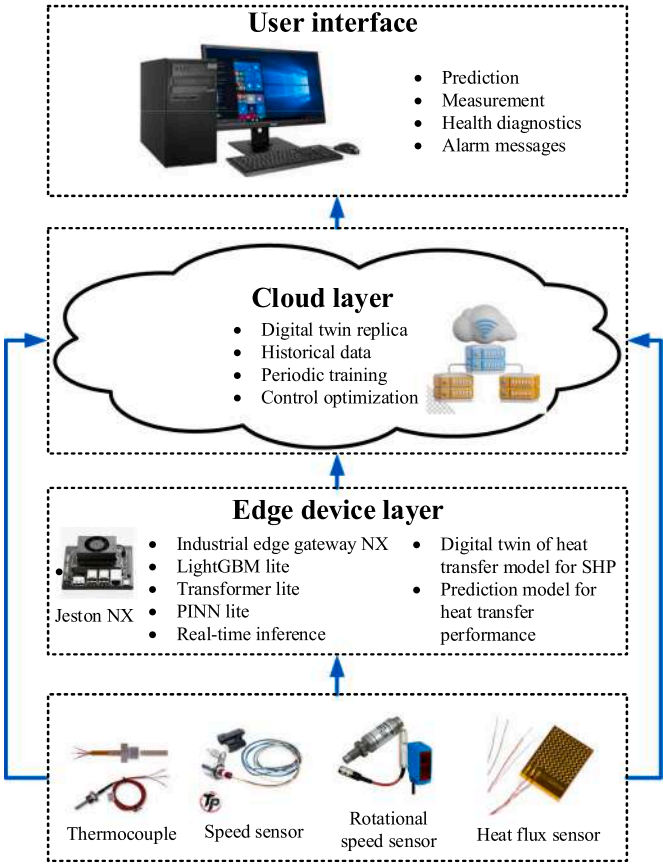

Fig. 26. Digital twin deployment framework for thermal error prediction and compensation in precision motion systems, integrating multi-layer AI modules across cloud, edge, and device levels. The cloud layer handles global model training, cross-device knowledge aggregation, and system-level optimization. The edge layer performs lightweight inference, data preprocessing, and local decision-making using compressed models (e.g., Transformer, LightGBM), while communicating with cloud services via MQTT or HTTP protocols. The device layer interfaces directly with physical sensors and actuators, enabling real-time feedback control. Seamless data flow and task scheduling between layers ensure low-latency prediction, adaptive model updating, and robust deployment in complex industrial environments.

4.1. Application deployment architecture

Although the focus of this study is on the thermal prediction of SHP rather than control, real-world SHP devices operate under dynamic and long-term conditions. The integration of a digital twin and cloud-edge deployment provides a flexible and scalable framework for continuously estimating and analyzing heat transfer performance under field conditions. The proposed system is structured in a three-layer architecture, including data acquisition (sensor/device layer), edge inference, and cloud management. Thermal and motion data are collected in real-time via NI cDAQ modules and transferred through A Guide to message queuing telemetry transport (MQTT) protocol to the edge device (NVIDIA Jetson Xavier NX), where the compressed prediction models are deployed. The cloud layer, hosted on a local server, is responsible for visualization, logging, and remote model update.

The proposed edge-cloud deployment framework integrating the AI prediction models into a digital twin-based SHP thermal management system is illustrated in Fig. 26. Sensor data from embedded hardware are streamed to edge nodes (e.g., industrial gateways) for real-time inference using compressed models (LightGBM, Transformer, or PINN). Longer-term optimization, anomaly detection, and retraining pipelines reside on cloud servers. The core modules include: (1) Sensor layer is responsible for the collection of the wall temperature, heat input,

pressure, and rotation sensors. (2) The edge device layer embeds the lightweight runtime engine hosting quantized LightGBM, Transformer, or PINN models. The cloud layer includes digital twin replica, offline retraining pipelines, data archiving and control optimization logic. The user interface is a web-based dashboard showing predicted vs. actual data, health diagnosis, and fault alert. In this architecture, the digital twin acts as a synchronized surrogate model, driven by both simulated dynamics (Simulink-based) and AI-enhanced predictions. Edge devices run lightweight prediction models (e.g., LightGBM or Transformer Lite) to support real-time thermal monitoring, while cloud servers manage historical data analysis, periodic retraining, and model optimization. Unlike control-oriented digital twin frameworks, the present system focuses on performance characterization and degradation tracking. This allows for reliable thermal modeling across long-term deployments, especially in industrial contexts where high-accuracy thermal components like SHPs are exposed to time-varying workloads. The deployment architecture was designed to ensure real-time response (<200 ms latency) and reduce the need for frequent cloud communication. On-device LightGBM inference supports anomaly pre-screening, while cloud servers handle weekly retraining based on accumulated thermal drift. In a practical use-case from spindle motor cooling system, Transformer Lite is deployed on an NVIDIA Jetson NX edge device, with latency measured below 150 ms under 20 Hz sampling rate.

All edge components communicated with the cloud using MQTT protocol under a publish-subscribe paradigm, coordinated by a central broker running on the cloud server. Latency measurements include end-to-end inference time from sensor data ingestion, model processing, to actuation signal generation. These deployment and runtime configurations are crucial for interpreting the inference latency, model footprint, and energy efficiency reported in Section 4.2.

4.2. System validation

The edge-deployed ANN surrogate reproduces the nonlinear transient behavior of the two-phase flow with a computation time two orders of magnitude shorter than that of the full SIMSCAPE solver, validating its advantage for real-time digital-twin applications. The integration of a physics-based digital twin and data-driven intelligence enables physically interpretable, real-time modeling, bridging the gap between detailed thermal-fluid simulations and edge-level control applications. To better evaluate model performance under varying transient conditions, three test scenarios are designed: (1) step increase in heat input (10 W to 30 W), (2) ramp-up in rotational speed (500–1500 r/min), and (3) combined fluctuation in both. To comprehensively evaluate model performance under transient conditions, a comparative analysis is conducted across three test scenarios: step increase in heat input, ramp-up in rotational speed, and combined fluctuations in both parameters, as shown in Fig. 27. Horizontally, PINN consistently exhibits the lowest prediction errors across all scenarios (0.85 °C, 0.90 °C, and 0.88 °C), indicating superior robustness in capturing physics-driven thermal responses. Transformer follows closely, particularly under steady or mildly dynamic conditions, with errors ranging from 0.89 °C to 0.95 °C. LightGBM, by contrast, shows the highest errors (1.20–1.35 °C), reflecting its limited ability to generalize over time-dependent features due to the absence of temporal modeling. Vertically, the error variation within each model reveals that PINN handles high thermal inertia (step input) most effectively, while Transformer performs better during smoother transient periods (ramp speed and combined fluctuations). These results highlight the strength of PINN in scenarios with strong physical coupling and the advantage of Transformer in maintaining stable accuracy under moderate dynamics. Results indicate that PINN outperforms Transformer in conditions with strong thermal inertia, while Transformer shows better average error across steady-state periods. The deviation observed in LightGBM is primarily due to the model's weaker capacity to generalize over temporal correlations.

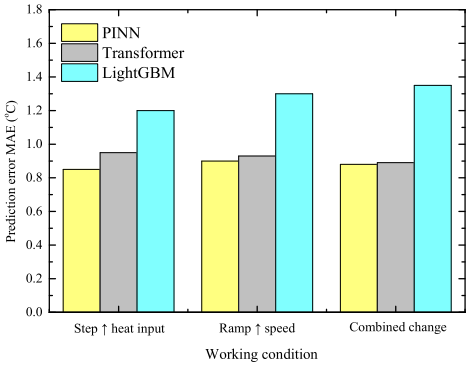

Fig. 27. Prediction error comparison of LightGBM, Transformer, and PINN models under three transient test scenarios: (i) step increase in heat input, (ii) rotational speed ramp-up, and (iii) combined fluctuation. Mean absolute error (MAE) is used as the evaluation metric. PINN exhibits the lowest error in case (i), benefiting from its embedded physical constraints that enhance robustness against sudden thermal changes. Transformer outperforms others in case (ii) due to its temporal attention mechanism, which captures gradual system dynamics effectively. LightGBM shows consistently higher errors, particularly under complex coupled fluctuations, indicating its limited ability to generalize beyond training conditions. These results highlight the importance of model architecture selection for dynamic thermal environments.

To comprehensively evaluate the performance and real-time capabilities of the proposed predictive framework, all models are deployed and benchmarked in a hybrid edge-cloud environment that mirrors typical industrial setups. The edge deployment is carried out on an NVIDIA Jetson Xavier NX platform, equipped with a 6-core ARM Cortex-A57 CPU, a 384-core Volta GPU with 48 Tensor Cores, and 8 GB of LPDDR4x RAM. This device is selected to emulate resource-constrained, real-time edge inference scenarios. The cloud-side computations are executed on a high-performance server with an Intel Xeon Silver 4314 CPU, 128 GB RAM, and an NVIDIA RTX 3080 GPU (10 GB GDDR6X memory), supporting model training, long-term storage, and digital twin synchronization.

Sensor data acquisition is conducted via NI cDAQ-9178 data acquisition hardware interfaced with LabVIEW 2021, enabling multi-channel analog input (e.g., thermocouples, heat flux sensors, encoder signals) with sampling rates up to 10 kHz. The system uses Python 3.10 with PyTorch 2.0 and LightGBM 3.3.5 for model execution. For deployment optimization, the Transformer model is converted into open neural network exchange (ONNX) format and quantized using TensorRT 8.5 for edge-side inference, achieving a significant reduction in latency. LightGBM is deployed as a serialized binary model and invoked via liblightgbm *C++* API, while PINN is containerized using Docker and executed via a PyTorch runtime with graphics processing unit (GPU) support.

The total system latency is

$$T_{total} = T_{acq} + T_{proc} + T_{comm} + T_{sync} \tag{51}$$

where T_{acq} is the sensor data acquisition delay; T_{proc} is the inference time depending on the model complexity; T_{comm} is the network communication delay; and T_{sync} accounts for asynchronous queuing or synchronization delays (e.g., MQTT buffering). This equation forms the foundation for comparing system architectures under different hardware and communication constraints.

To relate model structure with inference efficiency, the processing time can be approximated by

$$T_{proc} \propto \nu \cdot FLOPs + \lambda \tag{52}$$

where *FLOPs* is the number of floating-point operations required by the model; ν is a hardware-dependent scaling factor; and λ represents fixed initialization or loading overhead.

For example, Transformer models scale with $O(N^2)$ due to self-

attention layers, while PINNs often involve iterative numerical solvers for embedded differential operators, resulting in higher computational cost. To quantify model efficiency under resource constraints, the real-time inference index is introduced.

$$R_s = \frac{1}{T_{proc} \cdot M_m} \tag{53}$$

where M_m is the model memory size (in MB). Higher R_s values imply better real-time responsiveness per unit resource.

System stability under burst input or high sampling frequencies can be characterized by the processing margin.

$$\Delta T_{system} = T_{cycle} - T_{total} \tag{54}$$

where T_{cycle} is the control loop sampling period. For the system to maintain real-time responsiveness,

$$\Delta T_{system} \geq \delta \tag{55}$$

where δ is the minimal margin (e.g., 50 ms) required for safe feedback control. If $\Delta T_{system} < 0$, delay accumulation or prediction backlog may occur, leading to degraded control performance.

The real-time response factor is

$$RFT = \frac{T_{total}}{T_{threshold}} \tag{56}$$

The throughput under burst input is

$$\eta = \frac{N_{frames}^{processed}}{N_{frames}^{input}} \tag{57}$$

In addition to predictive accuracy, deployment-related metrics are evaluated, including inference latency, model size, and steady-state MAE (Fig. 28). LightGBM achieves the lowest inference delay (80 ms) and the smallest model footprint (9 MB), making it suitable for resource-constrained environments. However, this comes at the cost of accuracy. PINN, while most accurate, shows the highest computational overhead. Transformer offers a balanced trade-off, with moderate latency (150 ms), compact model size (36 MB), and acceptable accuracy, positioning it as the most deployment-efficient candidate in edge-cloud architectures. In addition to the average prediction accuracy, the temporal stability of each model under non-periodic thermal loads is analyzed. PINN exhibits minimal oscillation and superior convergence behavior, as reflected by its smooth loss reduction and bounded physics residuals, whereas the Transformer occasionally shows fluctuation in convergence under irregular inputs. Deployment efficiency is further assessed by measuring the end-to-end response latency across different architectures. The edge-deployed LightGBM model demonstrates a minimal memory footprint (under 10 MB) and inference delay below 100 ms, but its accuracy is compromised. In contrast, the distilled Transformer Lite model balances accuracy and latency effectively, making it suitable for real-time control integration. To further analyze the computational demand of each model, the number of floating-point operations (FLOPs) is estimated as a proxy for model complexity. As shown in Fig. 28, the PINN has the highest computational burden, with an estimated 2.2 billion FLOPs per inference due to the inclusion of embedded differential solvers and multi-pass residual evaluation. In contrast, the Transformer model, while more complex than traditional machine learning approaches, requires only 750 million FLOPs thanks to efficient attention mechanisms and parallelizable matrix operations. LightGBM exhibits the lowest complexity, with just 180 million FLOPs, as it relies on structured decision trees without deep network layers. This comparison illustrates that PINN's superior accuracy comes at the cost of significantly higher inference latency, while Transformer provides a balanced trade-off between complexity and speed. LightGBM remains the most

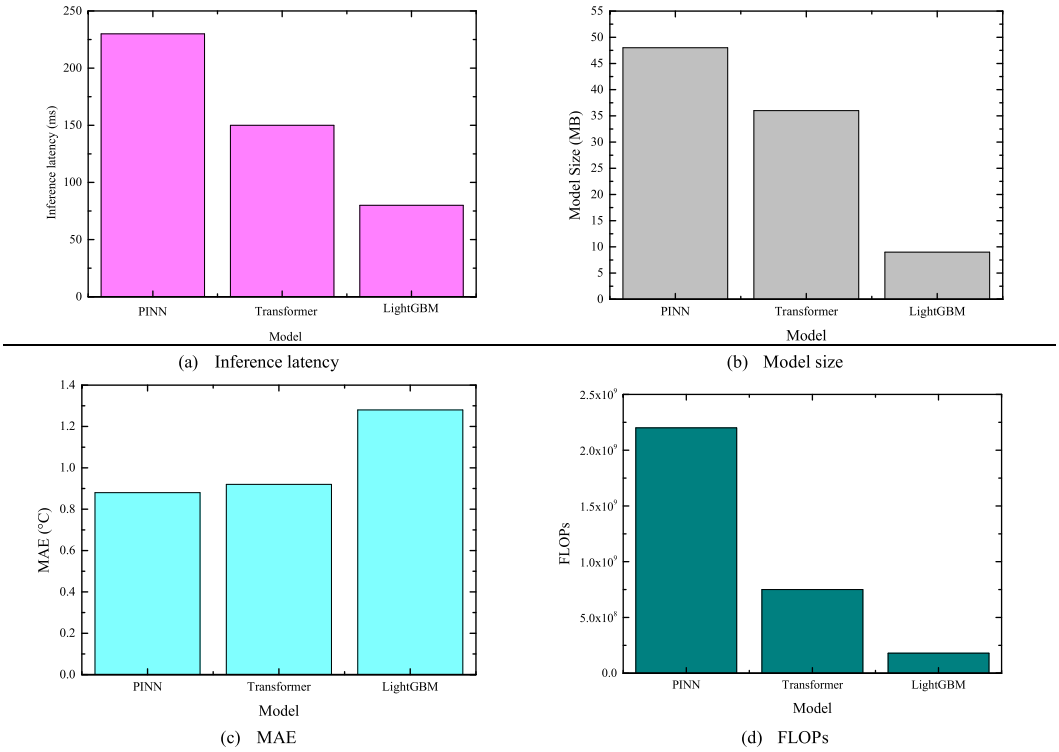

Fig. 28. System-level validation results of the proposed digital twin framework integrating heat pipe cooling, multi-model thermal prediction, and edge-cloud deployment. The figure shows temperature tracking performance and residual error over time during full-loop operation, including sensing, model inference, and compensation. The framework maintains tracking error within ±0.3 °C under dynamic thermal loads, demonstrating robust real-time capability. Edge-side inference latency remains below 150 ms, ensuring that compensation actions are triggered within acceptable control cycles. These results confirm the effectiveness and responsiveness of the proposed architecture for real-world thermal error mitigation in precision motion systems.

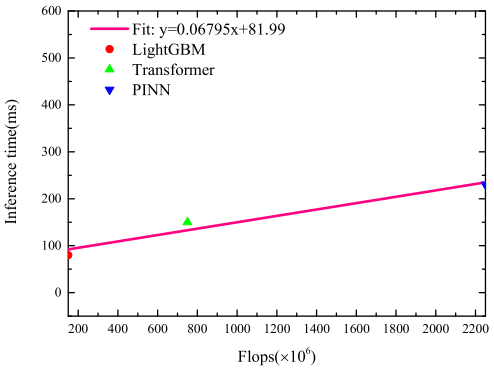

Fig. 29. Inference time comparison of LightGBM, Transformer, and PINN models, evaluated under identical hardware and deployment conditions. The total inference latency includes model loading, data preprocessing, and forward propagation time on an industrial edge device. LightGBM demonstrates the lowest inference time (~60 ms) due to its shallow structure and compact model size. Transformer maintains moderate latency (~100 ms), benefiting from efficient matrix operations and parallelism. PINN exhibits significantly higher inference time (~480 ms), attributed to the complexity of physics-constrained computation and residual evaluation. This comparison highlights the critical trade-off between model accuracy and deployment responsiveness in real-time thermal compensation systems.

computationally efficient, making it a suitable candidate for real-time edge deployment scenarios with limited hardware resources.

The relationship between model complexity and inference time is illustrated in Fig. 29, where the inference latency is plotted against the estimated FLOPs for three models. A linear fit of the form y=0.06795x+81.99 is obtained, indicating that inference time increases proportionally with computational complexity. Among the evaluated models: LightGBM, with approximately 1.8×10^8 FLOPs, achieves the lowest inference latency of around 94 ms. Transformer, with roughly 7.5×10^8 FLOPs, demonstrates a moderate latency of approximately 130 ms. PINN, the most complex model at 2.2×10^9 FLOPs, incurs the highest latency, exceeding 500 ms. This linear trend validates the use of FLOPs as a predictive metric for real-time feasibility. It also highlights the trade-off between model expressiveness and deployment latency, where PINN offers accuracy at the cost of speed, while LightGBM favors responsiveness with reduced complexity. Transformer offers a middle ground, achieving reasonable latency under edge-device constraints.

This framework enables proactive control of SHP devices under complex thermal loading conditions and supports fault-tolerant operations in industrial or aerospace applications. In summary, the AI-based regression framework provides a high-fidelity and low-latency complement to detailed simulations, supporting system optimization and control deployment. Experimental results and practical deployment framework further validate the feasibility and novelty of the proposed approach in real-world thermal system applications. The proposed hybrid modeling approach combines physically constrained SIMSCAPE simulations and data-driven learning to bridge the gap between high-fidelity modeling and real-time applicability. Experimental validation confirms the external accuracy, while model-inferred internal variables offer insight into the nonlinear transport behavior inside the rotating heat pipe.

5. Conclusion

Firstly, a high-fidelity digital twin model is developed in Simulink to simulate heat transfer of a sintered core heat pipe, incorporating realistic rotational thermal loads and contact conduction effects for reliable data generation and validation under both steady and transient conditions. Secondly, three predictive models-physics-informed neural network, Transformer, and light gradient boosting machine-are trained and evaluated, with the physics-informed neural network achieving the highest accuracy in strong thermal inertia scenarios (mean absolute error = 0.85 °C) and the Transformer demonstrating the best trade-off between accuracy and efficiency under steady states (root mean square error = 0.58 °C). Finally, the proposed edge-cloud artificial intelligence framework is deployed for real-time thermal modeling, achieving a response latency of 150 ms and compact model size (36 MB) after Turing Tensor R-Engine acceleration, confirming its feasibility for embedded implementation in intelligent precision motion systems.

Beyond its contributions to thermal prediction methodology, the proposed edge-cloud artificial intelligence framework for SHPs embodies a scalable, energy-aware paradigm that aligns with industry-level objectives for energy optimization. Continuous, real-time thermal prediction can greatly reduce parasitic energy usage in high-density electronics and aerospace systems. By integrating artificial intelligence directly into thermal control loops, this work supports the broader vision of artificial intelligence-enabled energy-conscious thermal system design. The proposed framework demonstrates strong potential for direct application in precision manufacturing systems where real-time thermal error awareness is essential. The experimental validations under various operational scenarios confirm that the modeling accuracy is sufficient for integration into feedback control loops, enabling proactive thermal compensation without additional sensor instrumentation.

CRediT authorship contribution statement

Jialan Liu: Writing – original draft, Visualization, Validation, Investigation, Formal analysis, Data curation. **Chi Ma:** Writing – review & editing, Writing – original draft, Validation, Supervision, Software, Resources, Project administration, Methodology, Investigation, Funding acquisition, Conceptualization. **Wenhui Zhou:** Validation, Investigation. **Mingming Li:** Validation, Investigation. **Jialong He:** Validation, Investigation. **Giovanni Totis:** Validation, Investigation. **Chunlei Hua:** Validation, Investigation. **Liang Wang:** Validation, Investigation. **Gangwei Cui:** Validation, Investigation. **Ruijuan Xue:** Validation, Investigation. **Zhi Tan:** Validation, Investigation. **Jun Yang:** Validation, Investigation. **Kuo Liu:** Validation, Investigation. **Yuansheng Zhou:** Validation, Investigation. **Jianqiang Zhou:** Validation, Investigation. **Shengbin Weng:** Validation, Investigation.

Declaration of competing interest

We declare that we have no financial and personal relationships with other people or organizations that can inappropriately influence our work; there is no professional or other personal interest of any nature or kind in any product or company that could be construed as influencing the position presented in, or the review of, the manuscript.

Acknowledgments

This research was supported by the National Natural Science Foundation of China (52275474, 52505541), the China Postdoctoral Science Foundation (2022M720565), and Open Research Project of the High-End CNC Machine Tool Key Laboratory at China General Technology (KLHCMT202404).

Data availability

Data will be made available on request.

References

[1] Han X, Wang X, Zheng H, Xu X, Chen G. Review of the development of pulsating heat pipe for heat dissipation. Renew Sustain Energy Rev 2016;59:692–709.
[2] Jafari S, Nikolaidis T. Thermal management systems for civil aircraft engines: review, challenges and exploring the future. Appl Sci 2018;8(11):2044.

[3] Bastakoti D, Zhang H, Li D, Cai W, Li F. An overview on the developing trend of pulsating heat pipe and its performance. Appl Therm Eng 2018;141:305–32.
[4] Mameli M, Besagni G, Bansal PK, da Silva RG. Innovations in pulsating heat pipes: from origins to future perspectives. Appl Therm Eng 2022;203:117921.
[5] Al-Obaidi AR, Alhamid J. Investigation of the effect of various corrugated pipe configurations on thermo-hydraulic flow and enhancement of heat transfer performance with the development of different correlations. Int J Therm Sci 2022; 176:107528.
[6] Wang X, Wright E, Liu Z, Gao N, Li Y. Development of a novel artificial neural network model for closed pulsating heat pipe with water and aqueous solutions. Asia-Pac J Chem Eng 2022;17(1):e2719.
[7] Kim W, Kim SJ. Fundamental issues and technical problems about pulsating heat pipes. J Heat Transf 2021;143(10):100803.
[8] Mameli M, Catarsi A, Mangini D, Recati A, Araneo L, Filippeschi S, et al. Start-up in microgravity and local thermodynamic states of a hybrid loop thermosyphon/ pulsating heat pipe. Appl Therm Eng 2019;158:113771.
[9] Kholi FK, Park S, Yang JS, et al. A detailed review of pulsating heat pipe correlations and recent advances using Artificial Neural Network for improved performance prediction. Int J Heat Mass Transf 2023;207:124010.
[10] Su Z, Li Z, Wang K, Kuang Y, Wang H, Yang J. Investigation of improved VOF method in CFD simulation of sodium heat pipes using a multi-zone modeling method. Int Commun Heat Mass Transf 2024;157:107669.
[11] Li G, Zhang Y, Zhang G, Huang S, Tang Y, Ding S, et al. Experimental investigation and numerical prediction on heat transfer performance of a high-speed radially rotating heat pipe. Case Stud Therm Eng 2024;62:105140.
[12] Chen H, Shi C, Yang L, Liu B, Zhao Q. Investigation of the droplet dynamics and thermal performance during dropwise condensation in the wickless heat pipe condenser. Int Commun Heat Mass Transf 2025;161:108487.
[13] Baraya K, Weibel JA, Garimella SV. A transient heat pipe model considering wick saturation effects that predicts dynamic evaporator dryout and recovery. Int J Heat Mass Transf 2025;242:126837.
[14] Wansasueb K, Promthaisong P, Bubphachot B, Pakkirat P, Saelim N. Applied machine learning: performance prediction of heat pipe with mesh wick. Case Stud Therm Eng 2024;63:105307.
[15] Jin IJ, Park YY, Bang IC. Heat transfer performance prediction for heat pipe using deep learning based on wick type. Int J Therm Sci 2024;197:108806.
[16] Bai X, Huang J, Chen Z, Liu J, Zhang Q. Predictive control of a heat pipe-cooled reactor based on a neural network model. Nuclear Eng Des 2025;436:113983.
[17] Qian N, Fu Y, Chen J. Thermal performance analysis of axial-rotating oscillating heat pipe and its prediction model based on grey system theory. Therm Sci Eng Prog 2022;29:101210.
[18] Jiang F, Qian N, Bernagozzi M, Fu Y, Chen J. Thermal performance prediction of radial-rotating oscillating heat pipe by a novel fusion model: a case study of application in grinding. Case Stud Therm Eng 2024;60:104731.
[19] Zhong R, Feng W, Ma Y, Wu T, Li L, Zhang Y. Experimental study of heat pipe start-up characteristics and development of an enhanced model considering gas diffusion effects. Appl Therm Eng 2024;257:124460.
[20] Ma Y, Zhang Y, Yu H, Li L, Feng X. Numerical modeling of alkali metal heat pipes. Ann Nucl Energy 2025;210:110855.
[21] Machado P, Pereira T, Trindade M, Santos A, Alves T. Estimating thermal performance of thermosyphons by artificial neural networks. Alexandria Eng J 2023;79:93–104.
[22] Kani GT, Ghahremani A. Predicting the thermal performance of heat pipes applying various machine learning methods and a proposed correlation. Int Commun Heat Mass Transf 2023;142:106671.
[23] Peh JS, Muhieldeen MW, Teng KH, Lim WH. A review on advancements in structural design of pulsating heat pipe. Therm Sci Eng Prog 2025;59:103361.
[24] Capolupo F, D'Alessandro C, De Maio D, Di Giamberardino F, Palmieri VG, Anacreonte AV, et al. Design and implementation of industrial hot pipeline prototypes with high vacuum multilayer insulation: enhancing thermal performance and lifetime. Appl Therm Eng 2025;264:125373.
[25] Cai S, Wang Z, Wang S, Perdikaris P, Karniadakis GE. Physics-informed neural networks for heat transfer problems. J Heat Transf 2021;143(6):060801.
[26] Zhao Z, Wang Y, Zhang W, Ba Z. Physics-informed neural networks in heat transfer-dominated multiphysics systems: a comprehensive review. Eng Appl Artif Intell 2025;157:111098.
[27] Faegh M, Ghungrad S, Oliveira JP, Rao P, Haghighi A. A review on physics-informed machine learning for process-structure-property modeling in additive manufacturing. J Manuf Processes 2025;133:524–55.
[28] Ma X, Li C, Zhan J, Zhuang Y. Physics-informed generative adversarial network solution to Buckley-Leverett equation. Math 2024;12(23):3833.
[29] Suh Y, Chandramowlishwaran A, Won Y. Recent progress of artificial intelligence for liquid-vapor phase-change heat transfer. npj Comput Mater 2024;10(1):65.
[30] Osorio JD, De Florio M, Hovsapian R, Chryssostomidis C, Karniadakis GE. Physics-informed machine learning for solar-thermal power systems. Energy Convers Manage 2025;327:119542.
[31] Dong W, Fu F, Shi G, et al. Hyperspectral image super-resolution via non-negative structured sparse representation. IEEE Trans Image (IN) Process 2016;25(5): 2337–52.
[32] Yao Q, Song D, Xu X. Robust finger-vein ROI localization based on the 3σ criterion dynamic threshold strategy. Sensors 2020;20(14):3997.
[33] Wang X, Li B, Yan Y, et al. Predicting of thermal resistances of closed vertical meandering pulsating heat pipe using artificial neural network model. Appl Therm Eng 2019;149:1134–41.
[34] Kalani H, Sardarabadi M, Passandideh-Fard M. Using artificial neural network models and particle swarm optimization for manner prediction of a photovoltaic thermal nanofluid based collector. Appl Therm Eng 2017;113:1170–7.
[35] Zhang X, Nikolayev VS. Physics and modeling of liquid films in pulsating heat pipes. Phys Rev Fluids 2023;8(8):084002.
[36] Sarkar D, Savory E, DeGroot C. Thermodynamic modeling of thermosyphons and heat pipes. Phys Fluids 2023;35:123307.
[37] Tower LK, Hainley DC. An improved algorithm for the modeling of vapor flow in heat pipes. In: Proceedings of the international heat pipe conference; 1989. NASA Tech. Memo NAS 1.26: 185179.
[38] Huber ML, Lemmon EW, Bell IH, Meng B, McLinden RA, Richter M, et al. The NIST REFPROP database for highly accurate properties of industrially important fluids. Ind Eng Chem Res 2022;61(42):15449–72.
[39] Tano Retamales ME. Modeling heat pipes with non-condensable gases. Idaho national laboratory report. Idaho Falls, ID, USA: INL; 2023.
[40] Hansel JE, Dutra CSB, Charlot L, Garcia AR, Craft AE, Clarno KJ, et al. The liquid-conduction, vapor-flow heat pipe model in Sockeye. Nucl Eng Des 2024;426: 113359.
[41] Bertsch SS, Groll EA, Garimella SV. Effects of heat flux, mass flux, vapor quality, and saturation temperature on flow boiling heat transfer in microchannels. Int J Multiphase Flow 2009;35(2):142–54.